Atmospheric response to removal of Southern Hemisphere sea ice

- a model study

Master Thesis in Geophysics Climate

Kristen Myklebust Ravnestad

June 2010

UNIVERSITY OF BERGEN
GEOPHYSICAL INSTITUTE

Picture on the front page: The Ross Sea.
Copyright John Weller (2010).
Downloaded from http://www.asoc.org/
Last visited: 24.05.2010
More information at http://www.lastocean.com/
Last visited: 30.05.2010

Acknowledgments

It has been five years of geophysical fun here at the Geophysical Institute. Thanks to my fellow students for making these five years so memorable.
Thanks also to Jonathan from Spotify. I do enjoy Spotify as much as you do.

Thanks to my advisor Nils Gunnar Kvamstø for all support and guidance. I have learned a lot from you. I would also like to thank my co-advisor Justin Wettstein. You taught me how to use MATLAB and were always available for consultation, regarding both interesting scientific problems and small annoying MATLAB issues. You have been super-awesome!

I would also like to thank my friends and family for all the support. At last a huge thank you to Ingunn for always getting me up in the morning and for being a counter-weight to the geophysics.

Kristen
Bergen, June 1st, 2010

Abstract

The atmospheric response to the removal of Southern Hemisphere sea ice is studied using the ICTP AGCM (SPEEDY) model with an uncoupled ocean. The results show large increases in surface heat flux from the ocean to the atmosphere over areas with sea ice removed. The increased heat flux is accompanied by an intense and shallow atmospheric warming in the annual and austral winter mean. Warming in the lower troposphere is associated with a positive geopotential height response that is usually equivalent barotropic. This atmospheric response is present in the annual and the austral winter means, with the largest magnitudes during the austral winter. A baroclinic pattern is found in the late summer (March) response. A comparison between the maximum theoretical local response and the model simulated response for September and March indicates a more non-local component of the response during March. A dipole response in the zonal wind field which is consistent with the geopotential height anomalies is found in the annual and austral seasonal mean. The eddy-driven midlatitude jet is weakened and shifted equatorward, while the subtropical jet is barely affected. Using empirical orthogonal function analysis, the Southern Hemisphere geopotential height variability has been investigated. A somewhat weaker Southern Annular Mode results within the simulation of removed sea ice and this result appears to be broadly consistent with the weaker eddy-driven jet.

Contents

Chapter 1

Introduction

The Earth is a planet in constant change, and the evolution of global climate is a part of this dynamical process. With the development of new technology along with various records, such as historical and paleoclimatological records containing information about past climate, we have been given insightful knowledge about these changes and processes. The global climate variability includes a set of natural cycles, and we distinguish between the terrestrial and non- terrestrial climate forcing. The Earth's orbital parameters and solar luminosity variation are examples of non- terrestrial forcing. The terrestrial forcing includes the release of natural aerosols due to e.g. volcanic eruption. Secondary forcings that appears as a result of climatic change could also be characterized as terrestial forcings. The terrestial and non-terrestial forcings are described in Hartmann (1994).

After the industrial revolution, the anthropogenic influence on global climate has gradually increased. The last 40 years there has been a significant (70 percent increase in concentration compared to pre-industrial levels) increase in the emission of greenhouse gases (GHG) due to human activity. Along with the known increase of 0.74^{o}C in the global average surface temperature in the 100 year linear trend between 1906 and 2004 (IPCC, 2007), this is could be interpreted as the anthropogenic influence on the global climate. The IPCC Fourth Assignment Report (AR4) also concludes a doubling of this temperature trend in high latitude regions. Such rise in atmospheric temperature would certainly have an impact on the polar ice caps.

Climate changes in high latitudes, and their influence on hemispheric and global climate, are mainly associated with sea ice and snow fraction variations. The main effect of the sea ice is a decrease in the amount of solar radiation absorbed by the oceans, due to its high albedo. Sea ice serves as a strong insulator, restricting exchanges of heat mass momentum and chemical constituents between ocean and atmosphere. Its presence affects the structure of the ocean-mixed layer and even deep circulation of the entire ocean (Washington & Parkinson, 1986). Changing processes that are connected to sea ice can trigger feedback mechanisms, which over time can increase or decrease the amount of sea ice. As the radiation budget at the surface is very sensitive to the sea ice extent, changes in the fractional ice cover could lead to positive and negative feedback processes, known as the ice albedo feedback (IAF). A more detailed description of the IAF is found in Hartmann (1994)).

Model runs studying the impacts induced by high latitude sea ice change have been performed. The impact of Antarctic sea ice, rather than that in the Arctic, could be considered because of the very dynamic nature of Antarctic sea ice, as it is located at lower latitudes, and because it is less confined by land masses than the arctic sea ice (Bromwich, 1998). The effect of changes in sea ice extent around the Antarctic continent

is not restricted to high latitudes, but also generates a substantial change in pressure, atmospheric circulation and precipitation in both hemispheres. This is shown in previous studies performed by Bromwich (1998) and Flugge (2009). Using the NCAR CCM2 model with a horizontal resolution of T42 (2.8^o latitude x 2.8^o longitude), Bromwich (1998) performed model simulations with all sea ice in southern hemisphere (SH) replaced by fixed SSTs of -1.9^{o}C. The procedure of using fixed SSTs was done to maximize the climatic response. By comparing a model run containing an ice free SH, with a control run with seasonal varying sea ice extent based climatological data and sea ice thickness of 2 m, the impact of SH sea ice removal was studied. The comparison between the two model simulations revealed a strong local surface warming around the coast of the Antarctic continent where the sea ice had been removed. Decreased sea level pressure and an increase in precipitation with a stronger convective component was found over areas with removed sea ice, and vice versa north of the former ice edge. The experiment also revealed changes in zonal wind, with a dipole response pattern (figure 1.1). Flugge (2009) performed a similar experiment using the AGCM ECHAM5 model, also with a T42 horizontal resolution. The sea ice in the SH was replaced by projected SSTs with a seasonal cycle included. In this experiment the SH sea ice thickness was set to 1 m. The local response in Flugge (2009) was an increase in the surface temperature over areas with removed sea ice, but in this experiment the decrease in sea level pressure over the areas with removed sea ice were not that significant. In agreement with Bromwich (1998), he discovered the dipole response pattern in the zonal wind.

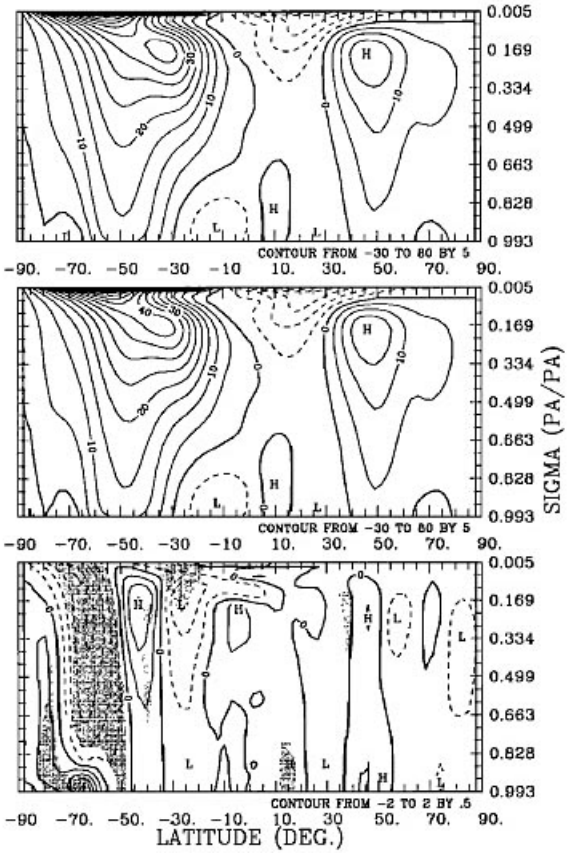

Figure 1.1: Latitude-height cross section of the zonal mean zonal wind response (m/s) from the experiment of Bromwich (1998). The control run (top), the perturbed run with removed sea ice (middle), and the response (bottom). A dipole response pattern in the zonal wind is The contour interval is 5 m/s. Figure from Bromwich (1998).

To understand the connection between global atmospheric responses to high latitude forcing, the linkage between the high-latitude, mid-latitude, and tropical circulations has been well studied. The linkage between high southern latitude climate and the tropics have been connected to the El-Nino-Southern Oscillation (ENSO) (Smith & Stearns, 1993; Garreaud & Battisti, 1999). It is also suggested that anomalies caused by removal of sea ice in the Antarctic region, could propagate into the Northern Hemisphere (NH) on a timescale of months (Bromwich, 1998). (Bader & Latif, 2005) also concluded that changes of SST in the Indian Ocean could affect the North Atlantic Oscillation (NAO) through the South-Asian jet.

In this thesis, the atmospheric response to removal of sea ice in the SH will be investigated. The main focus will be on the connection between the temperature (T) response and the geopotential height (GH) response. As the two studies of Bromwich (1998); Flugge (2009) shows different responses in the GH, the equivalent barotropic versus the baroclinic atmospheric response will be discussed. Which one is dominating in the

model simulations performed in this thesis? The degree of linearity and non-linearity of the circulation patterns connected to the response will also be studied, in addition to which amount the responses has a local or non-local character. General circulation models used for simulation of climate, including the NCAR CCM model used by Bromwich (1998), has been evaluated for their performances over polar regions Xu *et al.* (1990); Tzengo *et al.* (1993); Tzeng *et al.* (1994); Bromwich *et al.* (1994, 1995); Tao *et al.* (1996). From these evaluations, it has been found that the horizontal resolution is crucial for the accuracy of simulated features. The model used in this thesis has a T30 horizontal resolution. It will therefore be interesting to study the differences between findings in this thesis and the findings in Bromwich (1998); Flugge (2009).

Chapter 2 provides a presentation of the basic theoretical background. Chapter 3 presents the model used in the thesis, and in addition presents the experimental design and analytical methods. The SH climatology is presented at the beginning of chapter 4, which also includes the comparison between ERA-40 reanalysis and the model output data use for model validation. The results from comparisons between the control run and the experimental run with removed sea ice in SH is presented in chapter 5. Chapter 6 provides a discussion and conclusions based on the results found in chapter 5.

Figure 1.2 displays the Antarctic continent marked with some of the geographical names used in this thesis.

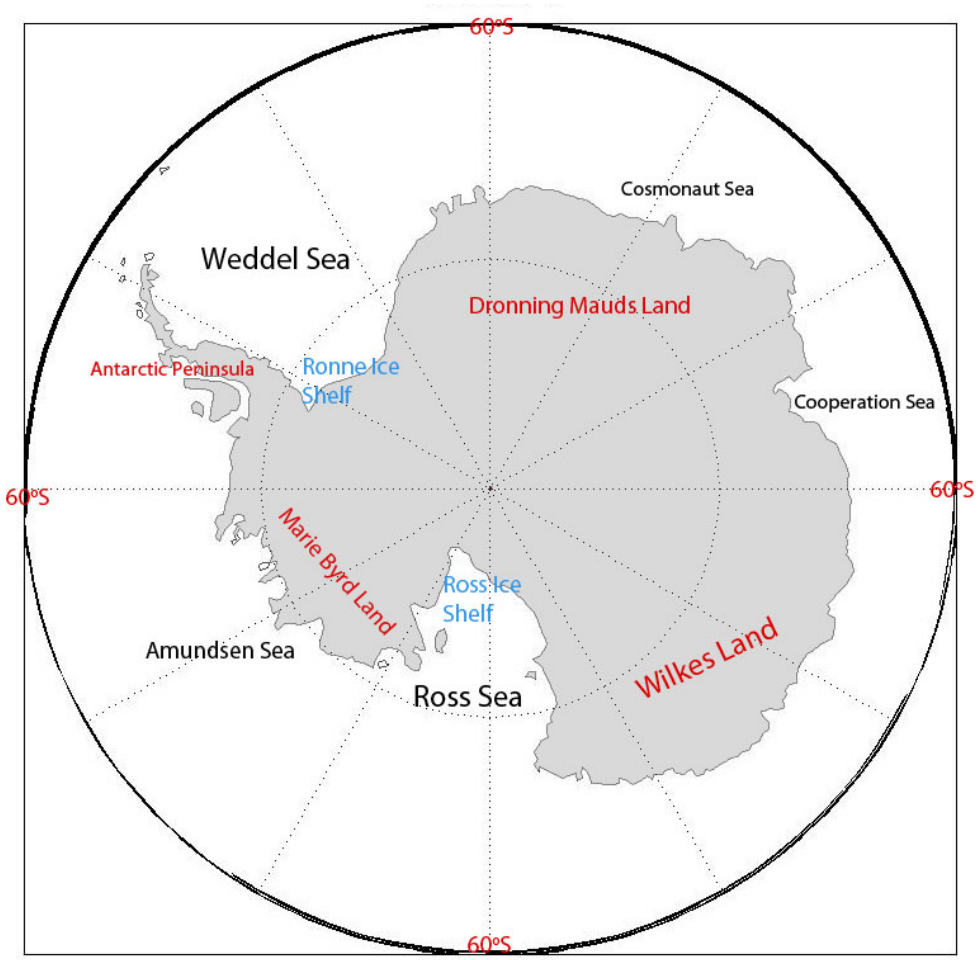

(a)

Figure 1.2: The Antarctic continent marked with some of the names on continental and ocean areas referred to in this thesis.

Chapter 2

Theoretical background

2.1 Effects of sea ice removal

The removal of the sea-ice creates significant changes in the local radiation budget. Less sea ice leads to more absorbed solar radiation, thus creating a warming of the ocean and increased ocean to atmosphere heat fluxes. This is a positive feedback mechanism known as the IAF (Hartmann, 1994). The fact that it is positive means that it strengthens itself during the process. Less ice leads to more absorbed solar radiation and warmer ocean, followed by less ice.

One of the main effects of sea ice removal is the warming of the near surface air due to increased heat fluxes between the sea and atmosphere. Such a response is shown in Bromwich (1998), where a simulation of an ice free southern hemisphere was compared to a control simulation containing boundary conditions set for the present climate. The large amount of surface warming is found locally over areas with removed sea ice (figure 2.1). This warming penetrates into the lower troposphere as a result of the hydrostatic instability. Depending on the type of dynamical response, surface warming will impose an atmospheric mass motion and affect the zonal wind in particular. This is shown by Bromwich (1998) where the results indicated a merging between the southern polar jet and the subtropical jet in the upper troposphere, in addition to decreased high latitude low level easterlies.

There are also a number of second-order effects connected to a decreased sea ice extent. There will be an increase of vertical (convective) circulation due to warming of the near surface air mass. The warmer lower air masses will be capable to hold more humidity, and when rising, causing convective precipitation. In the conclusion of Bromwich (1998) it is stated that the removed sea ice caused a greater component of convective precipitation over former sea ice covered areas. These changes was most dominant during the austral winter (May - September).

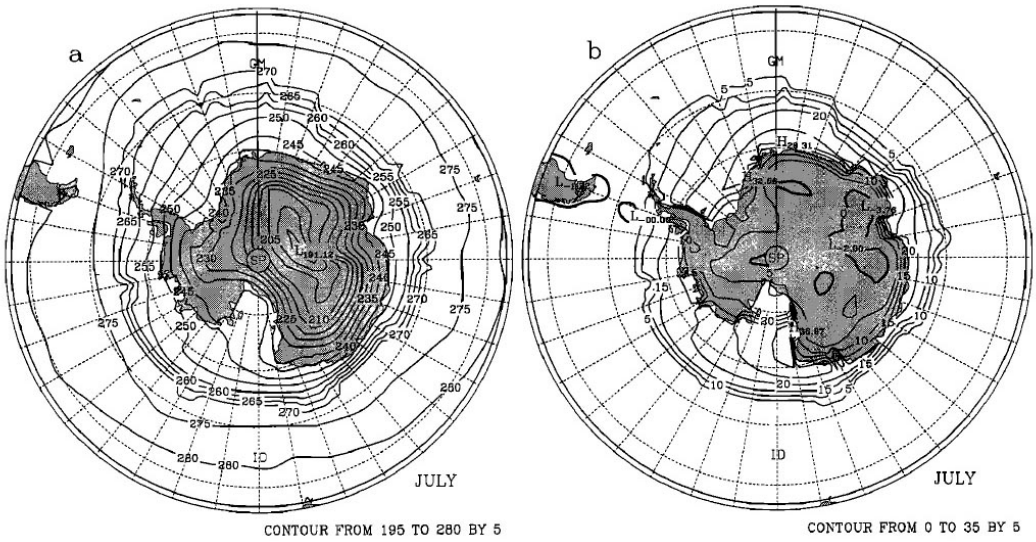

Figure 2.1: Time-averaged July surface temperature (K) for (a) the control simulation (CNT) and (b) the difference between the simulation without sea ice in the southern hemisphere (NSIS) and CNT for 90^{o}S-45^{o}S. The contour interval is 5 K. The thick contour is 0 K. Figure and figure caption from Bromwich (1998), where comparison between a sea ice free southern hemisphere and a control simulation were performed.

2.2 Linear and non-linear response to surface warming

With the presence of a thermal forcing such as surface warming, linear and non-linear responses will occur. Changes in the geopotential height and the thermal wind balance are some of the responses that could be induced by such a forcing. In this section the close connection between the temperature (T), geopotential height (GH) and the thermal wind will be described. Such a description could also be found in Fagerli (2008); Flugge (2009) and in Holton (2004).

The hypsometric equation 2.1 is derived from the ideal gas law and the hydrostatic equation.

$$h = z_2 - z_1 = \frac{R \cdot T}{g} \cdot ln\left[\frac{P_1}{P_2}\right] \tag{2.1}$$

P_1 and P_2 is the pressure in two different levels, T is the vertically averaged temperature, R is the gas constant for dry air, g the gravitation constant, z_1 and z_2 is the geopotential height related to the pressure surfaces P_1 and P_2. The geopotential difference between the two layers is given by h. It has been shown by Kushnir *et al.* (2002) how the atmosphere can respond to surface warming by means of the hydrostatic equation. Equation 2.1 can, as shown in Appendix A.2, be written as

$$Z'_{500} \approx \bar{Z}_{500}\left(\frac{T'_0}{T_a} + \frac{1}{ln2}\frac{p'_{surface}}{1000}\right) \tag{2.2}$$

which could be used to describe the connection between warming of near surface air masses and the linear response of the pressure surfaces. T'_0, $p'_{surface}$, $\bar{T}_a$, $\bar{Z}_{500}$ and Z'_{500} denotes the anomaly in the sea surface temperature, the surface pressure perturbation, the mean atmospheric T, the mean GH of the 500 hPa surface, and the perturbed GH of the 500hPa surface, respectively (Kushnir *et al.*, 2002). The equation consists of two terms. The first term is giving the baroclinic response, which contributes with up to 20 m for T'_0 = 1 K. The second term gives the barotropic response and will add or subtract 7 m for every 1 hPa perturbation (Kushnir *et al.*, 2002). It should be noted that the effect of the surface heat flux (SHF) on the local change of T, and the assumption that the lower atmosphere has come into thermal equilibrium due to this surface warming, is an overestimation (Kushnir *et al.*, 2002). The dynamical characteristics of a response of an atmospheric warming at midlatitudes includes a surface low downstream of the heat anomaly and a high aloft over the anomaly. This will generate circulation that weakens the hydrostatic response in the upper air. If midlatitude dynamical feedback are included, the surface pressure (SP) response may have the same sign as the GH response aloft(Kushnir *et al.*, 2002).

The thermal wind equation as defined in (Holton, 2004):

$$V_T = \frac{R}{f} ln \left[\frac{p1}{p2}\right] k \times \nabla_p \bar{T} \tag{2.3}$$

V_T is the generated thermal wind, R is the gas constant for dry air, f is the Coriolis parameter, p_1 and p_2 is representing two pressure surfaces, k is the vertical unit vector, and the last part represents the horizontal gradient of the mean temperature T between p_1 and p_2. Equation 2.3 is defined as the difference between the geostrophic wind (equation 2.5) at two pressure surfaces. The geostrophic wind is defined from an assumption of balance between the pressure and the coriolis force, hence it is directed parallel to the isobars. This is valid for large scale motions Wallace (1977). By subtracting the upper level geostrophic wind with the lower level geostrophic wind, the vertical wind shear between the two is found, which is defined as the thermal wind. The cross product between the vertical unit component and the horizontal temperature gradient in equation 2.3 means that the thermal wind always is at right angle to the temperature field, and parallel to the isotherms with warm air to the right. By this, equation 2.3 could be used to estimate the mean horizontal temperature advection in an atmospheric layer as seen in figure 2.2 (Holton, 2004).

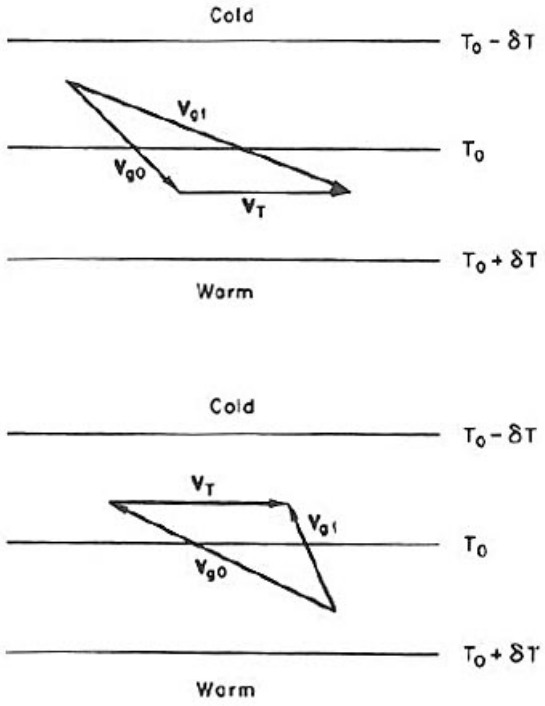

Figure 2.2: The relationship between the wind shear of geostrophic wind, the thermal wind, and the temperature advection. (top) cold advection and (bottom) warm advection. V_{g0} is the lower geostrophic wind and V_{g1} is the upper geostrophic wind. Figure from Holton (2004).

The notions barotropic and baroclinic could be explained using the thermal wind equation (Holton, 2004). Regarding barotropic situations, we distinguish between two states - equivalent barotropic atmosphere and barotropic atmosphere. In a barotropic atmosphere there are no horizontal temperature gradient present. The surfaces of constant pressure are coincident with surfaces of constant temperature. This corresponds to a geostrophic wind being independent with height, thus no vertical geostrophic wind shear is present. The equivalent barotropic atmosphere is a special case of the barotropic state where the horizontal temperature gradients exits, but the thickness and height contours are parallel everywhere (Wallace, 1977). This means that the geostrophic wind is dependent with height, but its direction is constant throughout the atmosphere. In a baroclinic atmosphere the density is allowed to change along the pressure surfaces. In other words, a horizontal temperature gradient exists, and given by the thermal wind equation 2.3, the geostrophic wind will change with height, both in direction and magnitude, generating a vertical geostrophic wind shear as seen in figure 2.2.

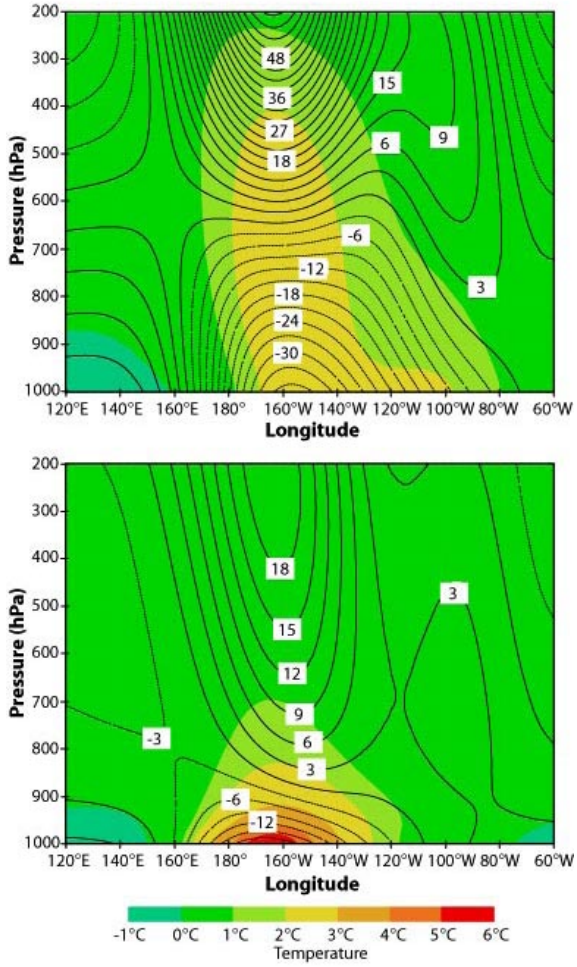

Figure 2.3: A linear quasi-geostropic model response to deep (top) and shallow (bottom) warming of the near surface air, in a wide β-channel and with a westerly baroclinic jet in its center. This is seen as a linear baroclinic response. The color shading indicates the perturbation temperature and the contours shows the geopotential height perturbation with a contour interval of 3 m. The warming decays exponentially with height and is centered around the date line (180^o. Figure 4 and caption from Kushnir *et al.* (2002).

Figure 2.3 shows the response of surface warming. Warmer air penetrates a certain distance into the atmosphere and decays exponentially with height, causing GH anomalies at the surface and aloft. The figure shows both deep (top) and shallow (bottom) warming, where the pressure anomalies indicates a surface low just downstream of the surface warming, and a high aloft. This response could be referred to as a downstream linear baroclinic response. Kushnir *et al.* (2002) notes that some simulations from General Circulation Models (GCM) indicates barotropic response to surface warming, making it necessary to include non-linear processes when evaluating such a situation.

This is shown in figure 2.4 where the induced convergent/divergent flow, and the corresponding secondary circulation are able to reverse the sign of the response. This could be explained by the quasi-geostrophic omega equation (equation 2.12).

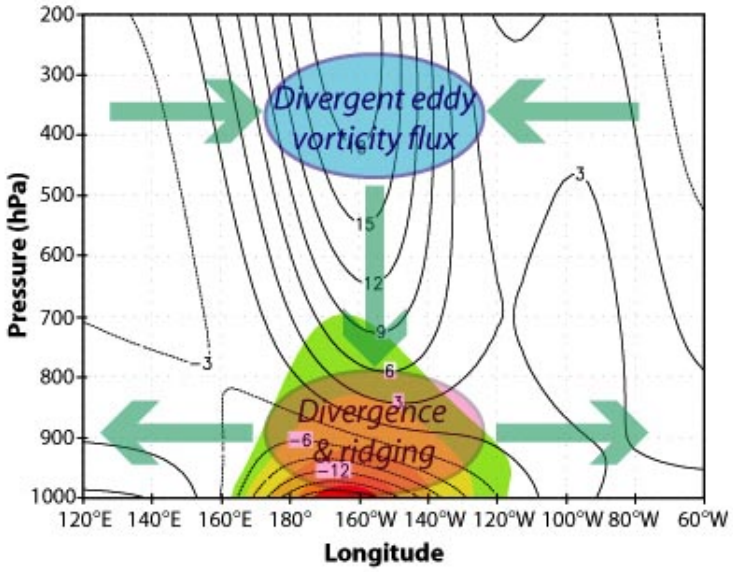

Figure 2.4: The response of shallow warming centered around 180^{o}. The geopotential response is indicated with lines with contour interval of 3 m. Temperature response is indicated with colors, with values smaller than 1K shaded white. The wide arrows shows the quasi-geostrophic secondary circulation that are induced as a result of eddy vorticity fluxes (colored eclipses) which are required by the heat transport. This is seen as a non-linear baroclinic response. Figure 5a from Kushnir *et al.* (2002)

2.3 Stationary waves forced by thermal anomalies

Thermal forcing could cause synoptic response in the atmosphere, but the extent to which thermal anomalies are able to induce large scale responses depends on their ability to create Rossby waves (Holton, 2004).

The following section about quasi-geostrophic theory, is based on the information found in Wallace (1977); Hoskins & Karoly (1981); Holton (2004); Fagerli (2008). When studying large scale motions, it is generally valid to assume the presence of hydrostatic balance and geostrophic balance. These two assumptions are given by the following equations in isobaric coordinates:

The hydrostatic balance:

$$\frac{\partial \phi}{\partial p} = -\alpha = -\frac{RT}{p} \tag{2.4}$$

This equation describes the upward force felt by an air parcel due to the vertical pressure force, and the gravitational force directed downward. $\phi = g_0 z$ is the geopotential and $\alpha = \frac{1}{\rho}$. R is the gas constant for dry air.

The geostrophic balance is given by

$$f\mathbf{k} \times \mathbf{V} = -\nabla\Phi \tag{2.5}$$

With the assumption of quasi-geostrophic balance, the following approximation can be made

$$\mathbf{V} \approx \mathbf{V}_g \tag{2.6}$$

Considering quasi geostrophic balance we assume the near balance between the Coriolis force and the horizontal pressure gradient. This is valid for large scale motions in the free atmosphere where the centrifugal force is neglectable, and where the horizontal pressure gradient force is relatively small, due to relatively weak horizontal pressure gradient. f is the Coriolis parameter and is associated with the Coriolis force. $\mathbf{V} = u\mathbf{i} + v\mathbf{i}$ and $\mathbf{V}_g = u_g\mathbf{i} + v_g\mathbf{i}$ denotes the real horizontal wind and the geostrophic wind, respectively.

Using the quasi geostropic potential vorticity equation, we are able to further study the implications of a thermal anomaly on the atmospheric circulation. This equation allows an investigation of the evolution in a quasi geostrophic flow. The quasi geostrophic potential vorticity equation is given by:

$$\frac{\partial \zeta_g}{\partial t} + \mathbf{V}_g \cdot \nabla \zeta_g + \beta v_g = f_0 \frac{\partial \omega}{\partial p} \tag{2.7}$$

This equation could be divided into 4 terms. The different terms describe the different physical effects in the equation. The first is the local change rate of geostrophic vorticity ($\zeta_g = \frac{\partial v_g}{\partial x} - \frac{\partial u_g}{\partial y}$). The advection of relative and planetary vorticity ($\beta = \frac{df}{dy}$) is given in the second and third term, respectivly. The last term is often called the stretching term and describes the change in relative vorticity due to the Coriolis force acting on convergent/divergent motions assosiated with ageostrophic motion ($V_a = V - V_g$). Here, the vertical velocity in pressure coordinates is given by $\omega \equiv \frac{Dp}{Dt}$. It should be noted that the last term often is written as $(f_0 + \zeta_g)\frac{\partial \omega}{\partial p}$, but for large scale motion (outside low pressure centers and frontal systems) usually $\zeta_g << f_0$, and therefore the relative vorticity could be neglected (Holton, 2004).

To get a full description of the non-linear structure in atmospheric motions, the thermodynamical effects must be considered. During adiabatic processes potential temperature is conserved (Wallace, 1977). The potential temperature is the temperature an air parcel will receive if it is moved from a level with pressure p to the surface with pressure p_0=1000 hPa (Wallace, 1977), and is given by the equation (often referred to as Poisson's equation):

$$\theta = T \left(\frac{p_0}{p} \right)^{\frac{R}{C_p}} \tag{2.8}$$

C_p is the specific heat of an air mass with constant pressure p and T is the temperature of the air parcel at pressure p. With the potential temperature being conserved during an adiabatic process, its state could be affected only by a diabatic heat source, such as a surface temperature anomaly. For this reason, the potential temperature is used in the thermodynamical energy equation:fic heat of an air mass with constant pressure p and T is the temperature of the air parcel at pressure p. With the potential temperature being conserved during an adiabatic process, its state could be affected only by a diabatic heat source, such as surface warming. Using potential temperature, the thermodynamical energy equation takes the form:

$$\frac{\partial \theta}{\partial t} + \mathbf{V}_g \cdot \nabla \theta + \omega \frac{\partial \theta}{\partial p} = \frac{Q}{C_p} \frac{\theta}{T} \tag{2.9}$$

The thermodynamic energy equation can also be divided into 4 terms. The first term describes the local rate of change in θ over time. The second term is the advection term and gives the change in θ due to horizontal advection. The vertical advection of θ is constrained by the vertical stability, and is given by the third therm. The last term describes the diabatic warming. This term is often called the forcing term and for an

adiabatic process Q=0, so the last term disappears. The last term describes diabatic processes in the atmosphere, such as latent heat release and surface warming.

The generation of Rossby waves is crucial for a local thermal forcing to induce non-local and large scale responses. Waves on this scale could be seen as anomalies from the zonal mean flow. It is therefore meaningful to linearize equation 2.7 and 2.9 around the zonal mean flow, in other words making it possible to describe any variable A by the sum of the zonal mean $\overline{A}$ and the deviation from this, A'. By applying this on the equations 2.7 and 2.9, we get the following set of equations, capable of being used in a discussion on the atmospheric adjustments to a thermal forcing, as done in Nigam & DeWeaver (2003).

The quasi geostrophic vorticity equation:

$$\overline{u}\frac{\zeta'}{\partial x} + v'(\beta - \frac{\partial \overline{u}}{\partial y \partial y}) = f_0 \frac{\partial \omega'}{\partial p} \tag{2.10}$$

The thermodynamic energy equation:

$$\overline{u}\frac{\partial \theta'}{\partial x} + v'\frac{\partial \overline{\theta}}{\partial y} + \omega'\frac{\partial \overline{\theta}}{\partial p} = \frac{Q}{C_p}\frac{\theta}{T} \tag{2.11}$$

The quasi-geostrophic potential vorticity equation (equation 2.7) can be used to estimate the vertical velocity ω, but it requires that the geopotential Φ and the change in the geopotential field $\frac{\partial \Phi}{\partial t}$ are known, and it does not use information from the thermodynamic equation (equation 2.9). The omega equation (equation 2.12), which utilizes both the vorticity equation and the thermodynamic equation, can be used as an alternative method to estimate ω. This equation is derived in Holton (2004) and is given as

$$\begin{aligned}\left(\nabla^2 + \frac{f_0^2}{\sigma}\frac{\partial^2}{\partial p^2}\right)\omega &= \frac{f_0}{\sigma}\frac{\partial}{\partial p}\left[\mathbf{V}_g \bullet \nabla\left(\frac{1}{f_0}\nabla^2\Phi + f\right)\right] \\ &\quad + \frac{1}{\sigma}\nabla^2\left[\mathbf{V}_g \bullet \nabla\left(-\frac{\partial \Phi}{\partial p}\right)\right] - \frac{\kappa}{\sigma p}\nabla^2 J\end{aligned} \tag{2.12}$$

2.4 Rossby waves

Planetary waves, or Rossby Waves are the most important wave type for large-scale atmospheric flow (Holton, 2004). As mentioned above, planetary waves could be seen as meridional deviations from the zonal mean flow. Such deviations, in form of a meridional velocity field, are induced by a perturbation vorticity. The perturbation of planetary vorticity is positive for a southward displacement and negative for a northward displacement. The meridional velocity field will advect the air parcels southward, west of the vorticity maximum and northward west of the vorticity minimum. Thus, the fluid parcels oscillate back and forth about their equilibrium latitude, and the westward propagating vorticity field relative to the background flow constitutes a Rossby wave (Holton, 2004).

As deviations from the mean flow with a meridional velocity component, the Rossby waves will change the planetary vorticity for an air parcel following the wave. Considering the initial state of the air parcel being advected along a latitude, ∂y is the meridional displacement of the parcel. The absolute vorticity η is given by $\eta = \zeta + f$, where ζ is the relative vorticity and f is the Coriolis parameter. Considering two time steps with t_0 being the initial time step at which $\zeta = 0$. In the second time step t_1, a meridional displacement ∂y is present (Holton, 2004). From the absolute vorticity, for t_1

$$(\zeta + f)_{t1} = f_{t0} \Rightarrow \zeta_{t1} = f_{t0} - f_{t1} = -\beta \partial y \tag{2.13}$$

$\beta \equiv \frac{\partial f}{\partial y}$ is the planetary vorticity gradient at latitude of the initial background state. The westward propagation of the Rossby wave is given by $c = \frac{-\beta}{k^2}$. This relationship yields that the phase speed is westward relative to the mean flow and is inversely proportional to the square of the zonal wave number k (Holton, 2004).

Chapter 3

Experimental design and analytical methods

3.1 The ICTP AGCM/SPEEDY model

The model used for this study is the numerical Simplified Parameterizations primitivE Equation DYnamics (SPEEDY) model, developed at the International Center for Theoretical Physics (ICTP) in Trieste, Italy. Speedy is an Atmospheric General Circulation Model (AGCM) of intermediate complexity, relative to state-of-the-art earth system models. This allows for substantial savings on computational resources. The SPEEDY models biggest advantage its ability to provide a relatively simple and time saving simulation of the global circulation. In general, the model requires an order less in computation time compared to the more advanced AGCMs. This gives us the possibility to do long model runs, and to do more simulations to increase the validation of our experiment. It's also easier to do isolated studies on the effects of different forcings in the model. All information about the model is found in Kucharski & Molteni (2006).

3.1.1 The general background of SPEEDY

The fundamental prognostic variables are vorticity ($\zeta = \frac{\partial v}{\partial x} - \frac{\partial u}{\partial y}$), divergence ($\nabla \bullet \mathbf{V} = \frac{\partial v}{\partial x} + \frac{\partial u}{\partial y}$) , absolute temperature and the logarithm of surface pressure. The model output also includes several other variables. The time integration is using a "leapfrog" system (Kucharski & Molteni, 2006). The horizontal resolution employed here is a Gaussian grid with 96 X 48 calculation points (figure 3.1(a)). This resolution corresponds to a triangular spectral truncation with a total wave number of 30. This is refereed to as the T30 resolution, and is equal to a distance of 3.8^o between the grid points. The model divides the atmosphere into 8 vertical layers (figure 3.1(b)). The computations are conducted on sigma layers with values of 0.025, 0.095, 0.20, 0.34, 0.51, 0.685, and 0.95. The sigma coordinates are defined as $\frac{p}{p_s}$. The model also defines half layers, which can be seen as the boundary layers between the full levels. These half layers are defined at sigma values of 0, 0.05, 0.14, 0.26, 0.42, 0.60, 0.77, 0.90, and 1. The full levels in the output data are post-processed onto the 925, 850, 700, 500, 300, 200, 100, and 30 hPa pressure levels (Kucharski & Molteni, 2006). Output variables can be studied in each of the pressure levels. Over the model topography, of which some pressure levels is lower, the variable data is estimated for the underlying level surfaces by using values from the lowest model level above the topography in the model.

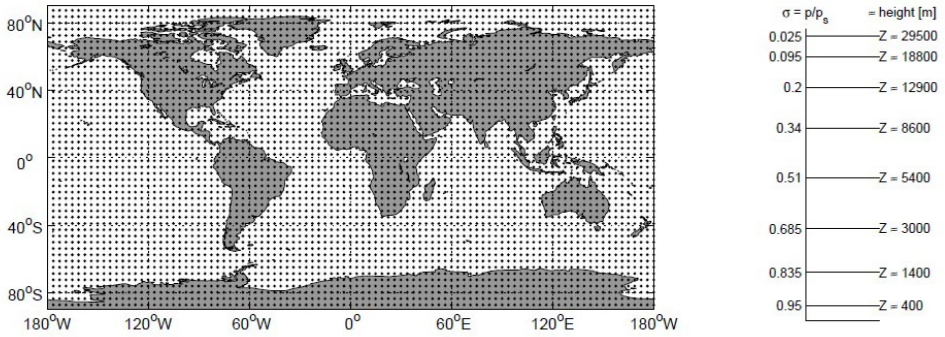

(a) (b)

Figure 3.1: The horizontal (a) and the vertical (b) resolution of the SPEEDY model. Figures from Fagerli (2008).

3.1.2 The Boundary Conditions

The boundary conditions used in SPEEDY are obtained from the ERA-15 reanalysis made by European Center for Medium Range Forecasting (ECMWF). This is a reanalysis of the climatological data over 15 years - from December 1978 to February 1994. The Sea surface temperature (SST) cycle is the monthly long term mean over the period from December 1978 to February 1994. Reanalyzes are produced using fixed, modern versions of the data assimilation systems developed for numerical weather prediction (ECMWF, 2009).

The variables included in the boundary conditions for SPEEDY are as listed in (Kucharski & Molteni, 2006):

- Sea surface temperatures (SST)
- Monthly sea-ice fraction,
- Monthly surface temperature in the top soil layer
- Moisture in the top soil layer
- Snow depth
- Bare surface albedo (when snow and ice is absent)
- The fraction of land/surface covered by vegetation

3.1.3 The Model Design and Physical Parameterizations

In the description of SPEEDY, Kucharski & Molteni (2006) gives a detailed description of the physical parameterizations in the model. These parameterizations are developed from basic principles used within more complex GCMs. The model has only one layer representing the stratosphere, which is meant to be a dynamic boundary layer, and the model code is set to reproduce the reanalysis temperatures in the lower stratosphere in this upper model layer. The surface fluxes in the model are calculated from standard aerodynamical formulas, but since the planetary boundary layer only is represented in the lowest of the atmospheric layers, we are not able to use the values of this layer to calculate the surface variables. It is also not possible to use the vertical gradient between two layers to estimate the stability. Therefore, the surface fluxes must be defined by doing approximations based on the values of the surface variables. The model is also producing skin temperatures for the different surfaces. Over land surface a simplification is made by assuming that the surface holds no heat capacity. When calculating the soil temperatures and the ice temperatures, the thickness of both ice and top soil are taken into consideration.

In addition, the model is implemented with a simple oceanic mixed layer. The use of such a mixed layer requires that the climatological boundary conditions for the heat fluxes are defined. This is defined as the SLAB ocean alternative.

3.2 Experimental Design

The model simulations in this thesis have been performed with the SPEEDY model. A simulation period of 51 year have been chosen, but for the analysis the first year of simulation has been removed. This is due to the spin up effect - the fact that the large scale motions takes time to settle, and it will provide more precise data for analysis. The analysis are based on 50 years of simulation.

For the experiments two model runs have been performed

- a control run (CTRL)
- an experimental run with all sea ice in SH removed(EXP1)

The CTRL run is based on climatological input from the ERA-15 reanalysis. This simulation is performed to give a reference run to the EXP1 run, and to validate the model output against the ERA-40 reanalysis described in section 4.2.1. In the EXP1 run, all SH sea ice has been removed and replaced with year round open water with fixed SSTs of

-1,5^{o}C. Bromwich (1998) also replaced the SH sea ice with fixed SSTs. A reason for replacing the sea ice with fixed SSTs instead of a more realistic projection of reduced sea ice, is that the climatic response will be maximized and the masking on the meteorological fields by the time variance in the model will be reduced Bromwich (1998). The SLAB ocean alternative is not used in my experiments. This means that the model-runs done for my thesis uses SST fields that do not interact back with the overlaying atmosphere during the model integrations. This gives us the possibility to reduce the complexity of the analysis of the response. The model runs have been performed on Parallabs Fimm supercomputers to get a shorter computing time (BCCS, 2010). The model output files are originally in grads format (.grd), but structured into time series and converted into MATLAB files (.mat) using scripts provided by Dr. Jürgen Bader. All analysis has been performed in MATLAB.

3.3 EOF analysis

Empirical orthogonal function (EOF) analysis is a useful tool to simultaneously investigate temporal and spatial variance patterns in a data set. Such analysis is widely used in geophysics and in analyzing numerical model simulations. In geophysics, the use of EOF analysis could be dated back to the 1950s when Lorenz (1956) developed a statistical technique to do weather forecasting based on such analysis.

The EOF analysis is a way to divide the variance in a dataset into different independent modes of variability. The modes describes patterns of anomalies in the spatial domain of the data set. Every EOF mode contains a corresponding eigenvalue that indicates how much of the total variance that can be explained. This is a common way to distinguish between different variability patterns in a dataset. The first mode, EOF1, explains most of the variance, thus it has the largest eigenvalue. The second mode, EOF2, explains second most and so on, subject to the constraint that all EOFs are spatially orthogonal to one another.

Each EOF pattern is associated with a unique time series - the corresponding principal component (PC). A large positive/negative PC value at a given time step indicates a large positive/negative amplitude in the corresponding EOF variability pattern at the given time step. Like the EOFs, the PCs are orthogonal correlated with one another.

For this thesis, an EOF analysis has been performed to study the variability in the 500 hPa GH field during June-July-August (JJA) - the austral winter. The analysis has been performed based on values from the SH (20^oS - 90^oS) and therefore matches the domain used to define the Southern Annular Mode (SAM) (Thompson & Wallace, 2000). The analysis is performed on JJA seasonal mean values calculated for the 50 years in both simulations. In addition to an EOF analysis of the 500 hPa JJA seasonal mean field for both the CTRL and EXP1 run, an analysis on the merged matrix of CTRL and EXP1 data has been performed. By doing this and comparing it with the individual simulation EOFs, it is possible to see if there is a shift in the mean of the JJA season for EXP1, compared to CTRL, and to investigate possible changes in the leading pattern of variability in the SH - the SAM.

Prior to the analysis, the following data formatting has been performed:

- JJA season is formed based on monthly-average results.
- The mean of the PC time series have been removed. This is done to be able to obtain the anomalies from the climatology of the pressure field.

- The PC time series has also been normalized by dividing each time series by its standard deviation.
- The data has also been weighted by $\sqrt{cos(latitude)}$ to fit the spherical form of the SH.

At last, the mean GH field at 500 hPa has been regressed onto the corresponding EOF1 by equation 3.1 to obtain the hemispheric-scale pattern associated with the PCs.

$$EOF1_{Z500} = \frac{\overline{X}_{Z500} \cdot PC1_{Z500}}{N} \tag{3.1}$$

$EOF1_{Z500}$ denotes the regressed EOF1 at 500 hPa, $\overline{X}$ represent the mean variable field corresponding to the EOF1, and PC1 is the corresponding standardized PC1. N is the number of data points in the time dimension of the analysis.

Chapter 4

Validations of the model

4.1 Southern hemisphere climatology

4.1.1 Southern hemisphere mean climatology

There are significant differences in mean climate between the southern hemisphere (SH) and the northern hemisphere (NH). A reason for this is the distribution of land and ocean in the two hemispheres. Compared to the NH, the SH has a much larger fraction of ocean surface. As a result there is a meridional temperature gradient and a distinct zonal wind pattern characteristic for each hemisphere due to the heat capacity of the oceans. In the SH, the large fraction of ocean surface causes less seasonal variance in the meridional temperature gradient. The relationship between the zonal wind and the hemispheric temperature field dominated by the meridional temperature gradient can, with high accuracy, be described by the thermal wind relationship given in equation 2.3 (Holton, 2004). Weaker meridional temperature gradient will weaken the thermal wind, thus weaken the strength of the zonal jet. As a result of this, the seasonal variance is smaller in the SH than in the NH where the boreal winter season is characterized by a strong zonal jet that disappears during the boreal summer due to warming from the midlatitude NH land masses. The large fraction of ocean surface in the SH, will also cause the topographic influence on the lower troposphere to be smaller than in the NH. In general, the SH zonal jet is far more zonally symmetric than the NH jet.

Based on data from the ERA-40 reanalysis, figure 4.1 shows a cross section of the zonal mean zonal wind in the SH. A year round strong subtropical zonal jet in the upper troposphere is characteristic for the SH with a midlatitude eddy driven jet extending all the way down to the surface over 50^oS. The eddy drive midlatitude jet is important in the transport of momentum polewards from the subtropical jet, and central in the development of high latitude storms. The core of the maximum zonal wind speed is called the mean jet stream axis, and describes the latitude where the thermal wind, given by equation 2.3, integrated through the troposphere is a maximum (Holton, 2004). During the austral winter season (JJA), the core of the subtropical jet is located around 30^oS, just at or below the tropopause on the southward flank of the Hadley Cell (figure 4.1(b)). The maximum wind speed in the jet core is >40 m/s. There is also a midlatitude eddy driven jet present during this season that extends from the surface to the upper troposphere over 50^oS. During the austral summer season (DJF) the subtropical jet decreases in strenght, moves southward to 50^oS and merges with the midlatitude eddy drive jet (figure 4.1(c)). During this season the jet core maximum wind speed is 30 - 35 m/s.

Figure 4.2(b) shows the spatial distribution of the SH zonal wind in 200 hPa for the JJA season. The subtropical jet is found in the South Indian Ocean and stretches as a

zonal band over the Australian Continent and into the west Pacific Ocean where it has its maximum. The DJF season (figure 4.2(d)) shows a southward shift in the subtropical jet and it merges with the eddy driven midlatitude jet, with a more zonally structure present. The maximum of the jet is also shifted towards the South Atlantic and south-west Indian Ocean sector. Figure 4.2(a) shows the spatial distribution of the SH zonal wind in 925 hPa for the JJA season. It is evident that the subtropical jet does not extend all the way down to the surface. The eddy driven midlatitude jet on the other hand has a maximum in the level located in the South Indian ocean. In DJF season (figure 4.2(c)) zonal wind has a more zonal structure and the jet in 925 hPa is located further north and could be seen as a near surface extension of the southward shifted subtropical jet/eddy driven jet.

The regions with largest zonal variability in the subtropical jet are found in the Pacific Ocean and over the Australian continent. The polar jet has the largest zonal variations in the region north of the Ross sea (Peters & Waugh, 2003). Zonal and meridional variations and the maximums in the upper tropospheric subtropical jet located between the western Pacific and the southeast of the African continent, have important influence on the Rossby waves in the SH. (Peters & Waugh, 2003).

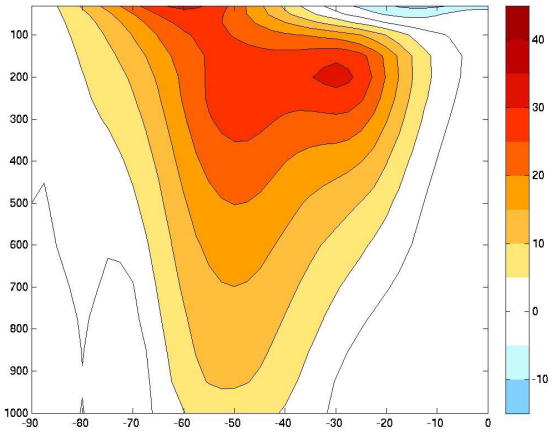

(a) Annual zonal mean

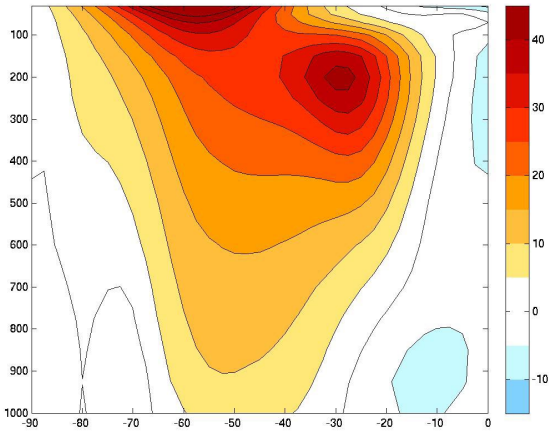

(b) Zonal mean JJA

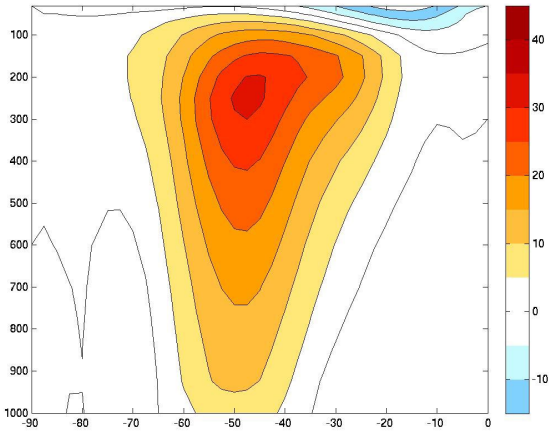

(c) Zonal mean DJF

Figure 4.1: Zonal mean zonal wind [m/s] for the annual mean (a), JJA seasonal mean (b), and DJF seasonal mean (c). Contour interval is 5 m/s. Figure based on data from the ERA-40 reanalysis.

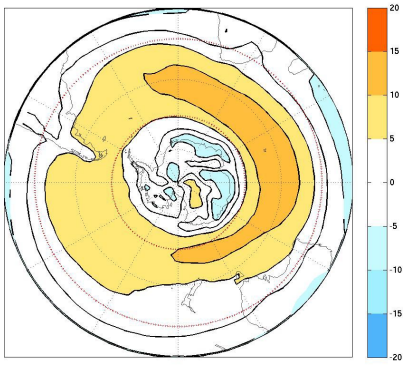

(a) JJA 925 hPa

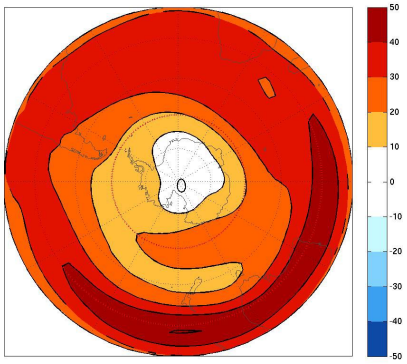

(b) JJA 200 hPa

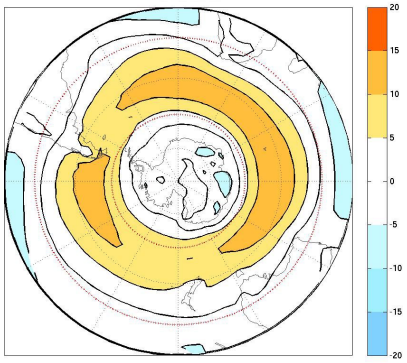

(c) DJF 925 hPa

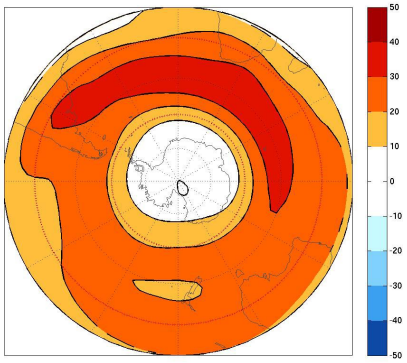

(d) DJF hPa

Figure 4.2: Mean zonal wind [m/s] for JJA in 925 hPa (a) and 200 hPa (b), and for DJF in 925 hPa (c) and 200 hPa (d). The Subtropical jet and the polar jet is marked in a and b. The contour interval is 5 m/s for 925 hPa, and 10 m/s for 500 hPa. Figure based on data from the ERA-40 reanalysis. 60^oS and 30^o are marked with a red dashed line.

4.1.2 Southern annular mode (SAM)

By preforming Empirical Orthogonal Function analysis (EOF analysis) on a data set it is possible to examine the large scale variability. In the SH, the mode that explains most of the large scale variability is called the Southern annular mode (SAM) (Limpasuvan & Hartmann, 1999; Thompson & Wallace, 2000; Arblaster, 2006), or often referred to as the High-latitude mode (HLM) (Kidson, 1988; Arblaster, 2006) or the Antarctic oscillation (AAO) (Rogers, 1982; Arblaster, 2006). The SAM is identified as the leading EOF when performing EOF on the monthly anomalies of the GH of 850 hPa, and it usually explains between 20-30% of the variance in a data set. It could also be identified in other variables and pressure levels as noted by Thompson & Wallace (2000). SAM represents fluctuations in the eddy-driven midlatitude jet. For zonal wind in the

austral winter SAM is assosiated with two different behaviours. We differ between the behaviour in the Indian Ocean sector and in the Pacific Ocean sector. Over the Indian Ocean, SAM is mainly assosiated with a latitudinal shift of the jet, while over the Pacific Ocean, the characteristics of SAM consists of a seesaw in the wind speed between distinct latiudes (Codron, 2007). A SAM in its negative phase is associated with an abcent eddy-driven midlatitude jet, and a stronger subtropical jet in the Pacific, and a SAM in its positive phase causes the eddy-driven midlatitude jet to shift poleward. In the Indian sector, an eddy-driven midlatitude jet is visible in both phases of SAM, and it just shifts poleward with the positive SAM (Codron, 2007). As anomaly patterns associated with SAM are changing with time as seen in standardized time series obtained by the PC of the EOF, we distinguish between positive and negative states of the anomalies. Positive/negative SAM corresponds to negative/positive pressure anomalies over the South Pole (Codron, 2007).

4.2 Mean climatology in the SPEEDY model

The SPEEDY model is able to create a realistic and accurate simulation of the global atmospheric circulation, in spite of its relativley simple structure. Some examples of comparisons between SPEEDY and more complex GCMs are available at the model web page (SPEEDY-Net, 2006).

4.2.1 ERA-40/CTRL-run

A comparison between the CTRL run and the ERA-40 reanalysis has been made to validate the output data from the model. The ERA-40 data set is made by ECMWF, and consists of reanalysis of the global climate in the time period of mid 1957 to 2001 - 45 years. It overlaps with the ERA-15 reanalysis which is the basis for the climatological input for the SPEEDY model. The horizontal resolution is a grid with 144×74 data points. The data set is downloaded from the ECMWFs web page (ECMWF, 2009).

To obtain plots of the difference between the model data and the reanalysis, the ERA-40 reanalysis data has been subtracted from the SPEEDY model data. This is done by using the "meshgrid" function in MATLAB. Since the model data and the ERA-40 data have different horizontal and vertical resolution, an interpretation between the two has been performed using the interp2 script in MATLAB. In the vertical, the SPEEDY output data contains 8 pressure levels from 925 hPa up to 30 hPa. For the ERA-40 data I have chosen all layers from 30 hPa and below - in all 16 pressure levels, when comparing cross sections. For the horizontal comparison I have picked out two levels

for analysis - 925hPa and 500 hPa. These levels has been chosen to give a comparison, both near the surface, and in the mid troposphere, and is also the levels used in the comparison between the CTRL and EXP1.

For a basic climatological comparison the geopotential height (GH), temperature (T), zonal wind (U), meridional wind (V) have been chosen as fundamental variables. It is evident that the model is projecting a higher GH in all areas at both 925 and 500 hPa (figure 4.3(a) and 4.3(b)). From the Antarctic continent and equatorwards to 60^oS there is a general overestimation from 50 m to 100 m in 925 hPa. The largest difference at this layer is found outside of Marie Byrds Land with magnitudes of the difference of 100 - 150 m (figure 4.3(a)). Over the Antarctic continent the GH difference is much bigger. In the 500 hPa layer an overestimation is found approximately over the same areas, but with higher magnitudes (figure 4.3(b)). In general the SPEEDY model is projecting a higher GH over areas with sea ice cover. The temperature field is well represented in both the 925 hPa and the 500 hPa level of the model, as seen in figure 4.3(c) and figure 4.3(d). In 925 hPa the temperature difference is negative over the polar ice cap. Further north, over the SH world oceans, the difference seems to be positive in general, with magnitudes between 2 - 4^oC.

The zonal wind has a dipole structure in the difference between the model and the reanalysis for the SH. This structure is present in both 925 hPa and 500 hPa (figure 4.4(a) and 4.4(b)) and seems to increase with height. Areas near the Antarctic coast and north of 30^oS seems to have a positive difference. In a zonal ring between 60^oS and 40^oS the model gives a weaker representation of the zonal wind with negative magnitudes up to -6 - -8 m/s in the South Pacific and the South Atlantic in 500hPa. For the meridional wind there are bigger deviations between the reanalysis and the CTRL in 925 hPa (figure 4.4(c)), than in 500 hPa (figure 4.4(d)). Outside of the western coast of the South American continent, figure 4.4(c) shows large negative difference between the ERA-40 data and the model data. This is probably due to the less detailed topography with smoothed contours.

Figure 4.5, 4.6, and 4.7 shows a comparison between cross-sections of the total annual zonal-mean from SPEEDY and ERA-40 and the difference between the two. The temperature profiles (figure 4.5) from SPEEDY and ERA-40 is very similar in its structure, at least in the low to mid troposphere. The difference between the two is found in the upper troposphere and the stratosphere (figure 4.5(c)). Here it is possible to see significant differences in the temperature with warmer air over the tropics and colder air over high latitudes. The zonal wind structure (figure 4.6) is also quite similar in low to mid troposphere. Here the biggest difference between the two is that the amplitude of the zonal wind jet is slightly weaker near the surface in the SH. In the upper

troposphere and the lower stratosphere, the model tend to over represent the zonal jet with larger values over the subtropics, and also projects weaker wind over the tropics (figure 4.6(c)). The double jet structure at upper levels seen in the ERA-40 reanalysis is not present in the model simulation, but instead replaced by a stronger merged jet. This could potentially lead to a weaker simulation of the SH JJA season jet structure, as the double jet structure is at its strongest during this season (figure 4.1(b)). The meridional wind pattern is well represented in the model, but with generally less amplitude as seen in figure 4.7. The Hadley Cell is present, though with weaker circulation.

In general, the model captures the overall climatological structures well in the troposphere. Noted by Xu *et al.* (1990); Tzengo *et al.* (1993); Tzeng *et al.* (1994); Bromwich *et al.* (1994, 1995); Tao *et al.* (1996), the horizontal resolution in crucial for the accuracy of the simulated features over polar regions. As seen in the GH field in figure 4.3(a) and 4.3(b), there are larger deviations from the reanalysis over the polar regions of the SH. The main weakness of SPEEDY is in its projection of the upper troposphere and the lower stratosphere. This is also mentioned by Molteni (2003). The stratosphere is only represented with one layer in the model (30hPa), which limits a detailed projection at such altitude. It is also stated that the model also underestimates the amplitude of the stationary waves Molteni (2003). Low level circulation is affected by the less detailed topography in the model. This is evident for the meridional wind, which often is induced by large mountain ranges. Over the tropics large differences in temperature is found. This could indicate a weakness in simulation of convective motion in the model, which also could cause a generally weaker Hadley Cell circulation and meridional winds. The estimation of low level variables over higher topography seems to generally overestimate the GH and under estimate T.

As the systematic errors in the SPEEDY model are assumed to be the same for both the CTRL simulation and the EXP1 simulation, the results from the two simulations described in chapter 5, will focus on the difference between the the two, and not the models deviations from the ERA-40 reanalysis.

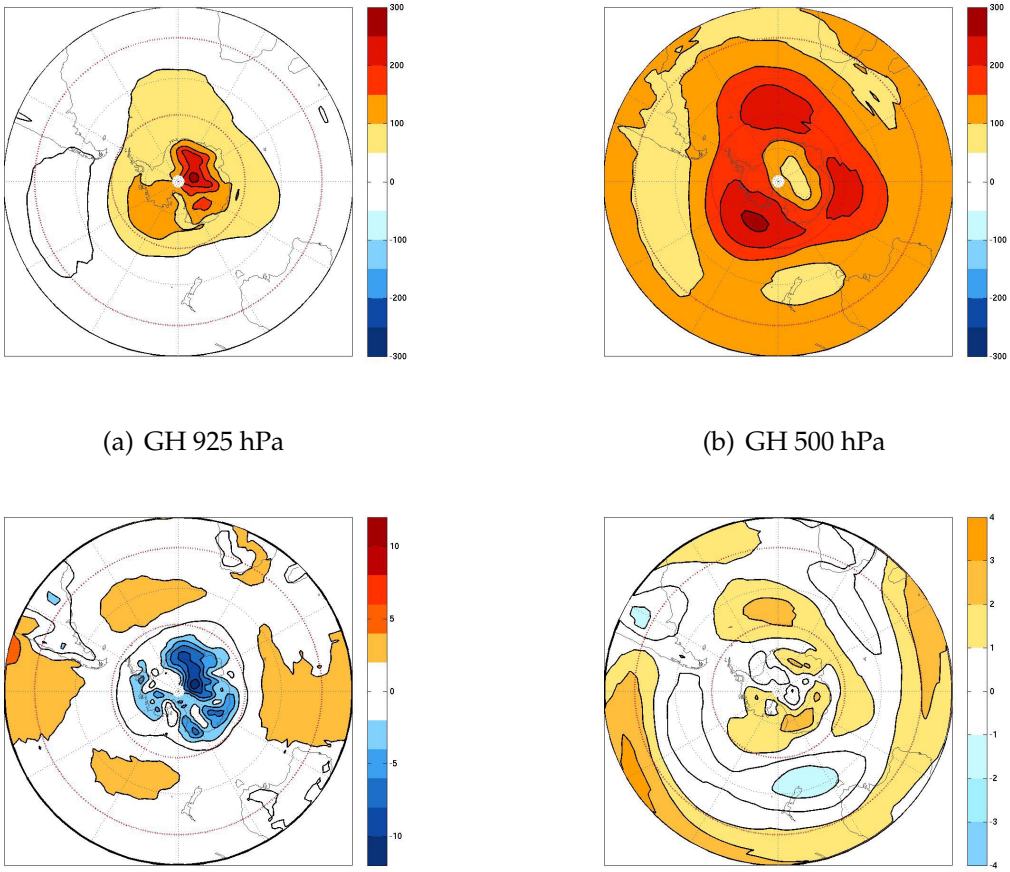

(a) GH 925 hPa

(b) GH 500 hPa

(c) T 925 hPa

(d) T 500 hPa

Figure 4.3: The difference between ERA-40 and the CTRL for the total annual mean. GH [m] at 925 hPa (a) (contour interval 50 m), GH [m] at 500 hPa (b) (contour interval 50 m), T [^{o}C] at 925 hPa (c) (contour interval 2^{o}C), and T [^{o}C] at 500 hPa (d) (contour interval 1 ^{o}C). 60^{o}S and 30^o are marked with a red dashed line.

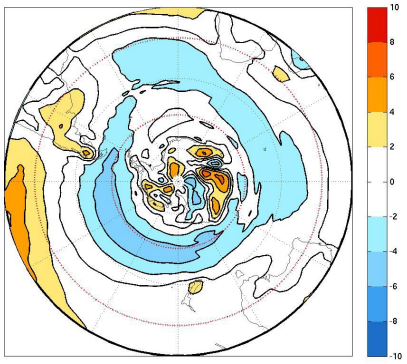

(a) U 925 hPa

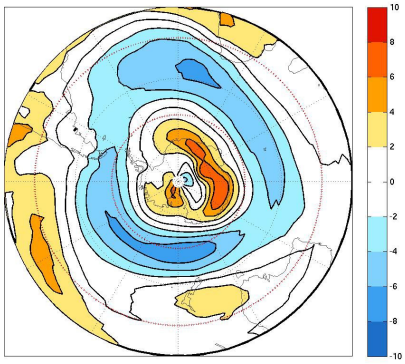

(b) U 500 hPa

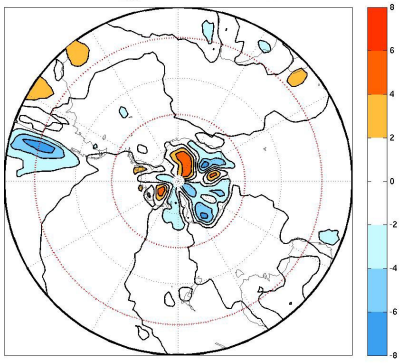

(c) V 925 hPa

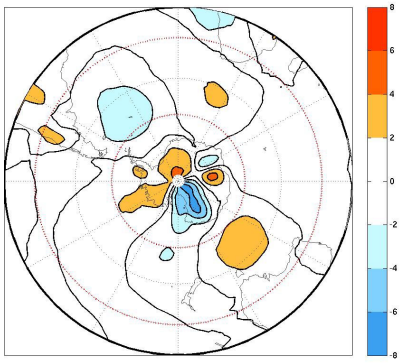

(d) V 500 hPa

Figure 4.4: The difference between ERA-40 and the CTRL for the total annual mean. U [m/s] at 925 hPa (a) (contour interval 2 m/s), U [m/s] at 500 hPa (b) (contour interval 2 m/s), V [m/s] at 925 hPa (c) (contour interval 2 m/s), and V [m/s] at 500 hPa (d) (contour interval 2 m/s). 60^oS and 30^o are marked with a red dashed line.

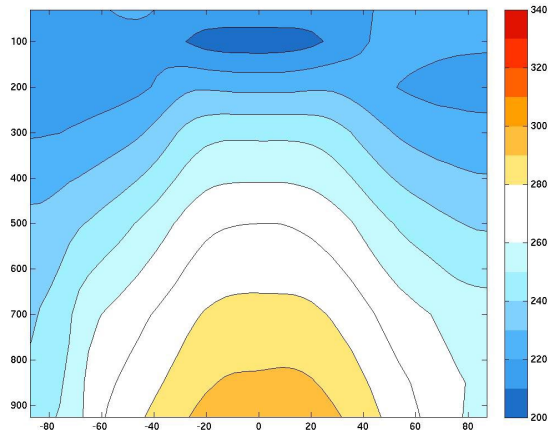

(a) SPEEDY T

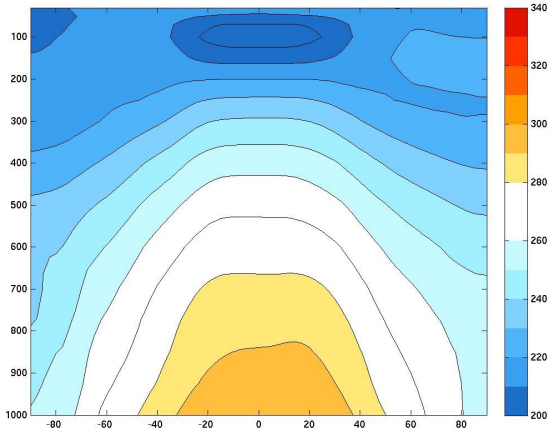

(b) ERA-40 T

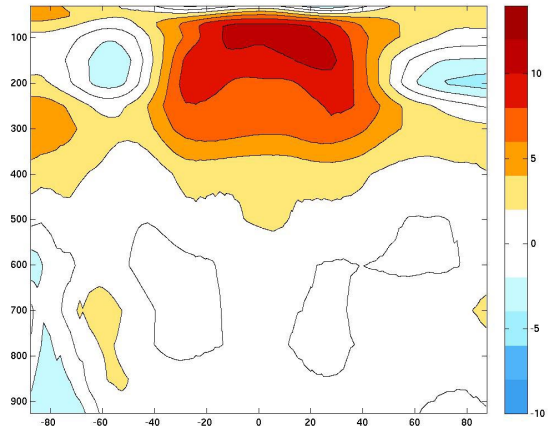

(c) Difference T

Figure 4.5: Cross section of temperature T [K] for the total annual mean, zonally averaged for the CTRL, ERA40, and the difference between the two data set (^{0}C). (a) SPEEDY, (b) ERA-40, and (c) the difference between the two. The center line within the white filled contour in (a) and (b) indicates 270 K. Contour interval is 10 K for a and b, and 2^{0}C in the difference.

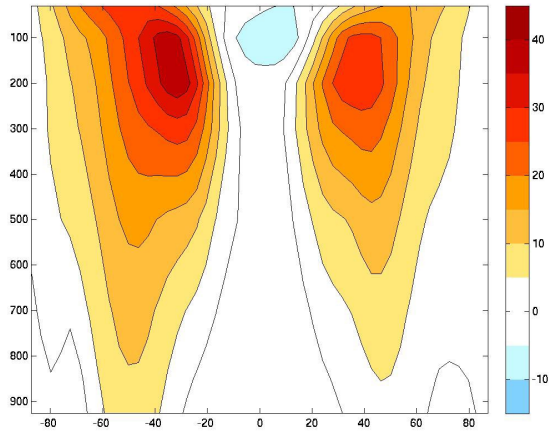

(a) SPEEDY U

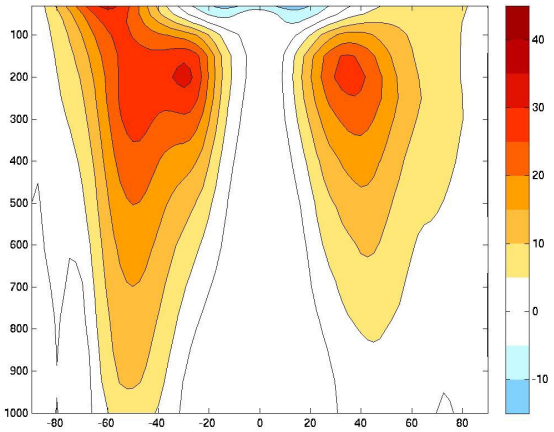

(b) ERA-40 U

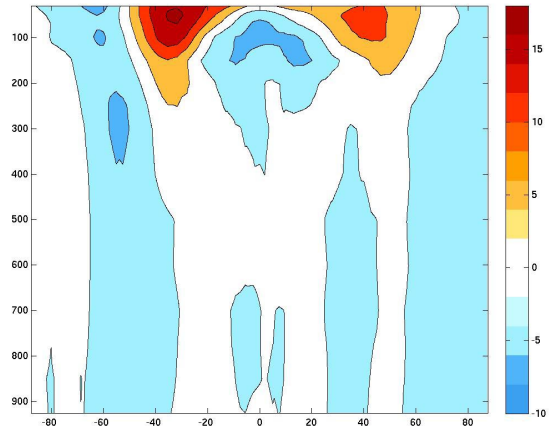

(c) Difference U

Figure 4.6: Cross section of zonal wind U [m/s] for the total annual mean, zonally averaged for the CTRL, ERA40, and the difference between the two data set. (a) SPEEDY, (b) ERA-40, and (c) the difference between the two. The contour interval is 5 m/s in a and b, and 2 m/s in c.

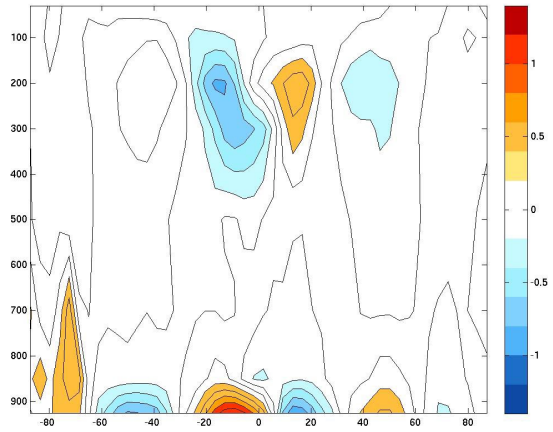

(a) SPEEDY V

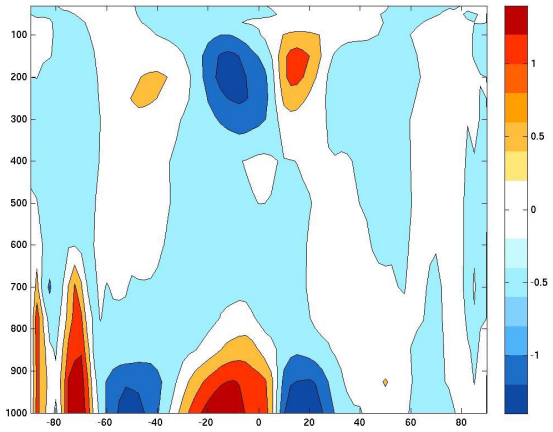

(b) ERA-40 V

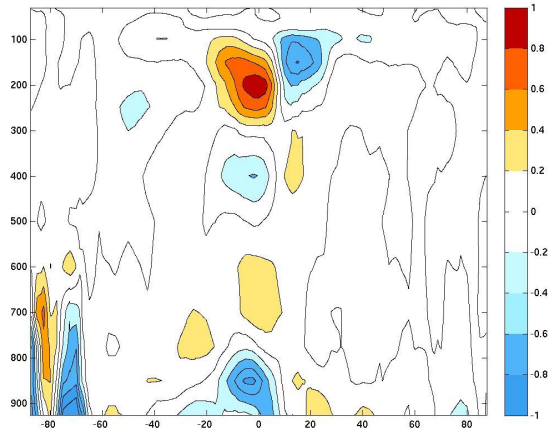

(c) Difference V

Figure 4.7: Cross section of meridional wind V [m/s] for the total annual mean, zonally averaged for the CTRL, ERA40, and the difference between the two data set. (a) SPEEDY, (b) ERA-40, and (c) the difference between the two. The contour interval is 0.2 m/s.

Chapter 5

Results

5.1 Introduction

This chapter will give a description of the results obtained by a comparison between the EXP1 simulation with SH sea ice removed, and the CTRL simulation. The most basic results describe the mean difference between the two model runs. This is done by subtracting the mean of the CTRL run from the mean of the EXP1 run. The difference between the two model simulations is defined as the response to the forcing. The response in surface heat flux (SHF), surface temperature (ST), and sea level pressure (SLP) is presented at the model's surface. Geopotential height (GH) and temperature (T) are presented at two levels - 925hPa and 500 hPa. The zonal wind (U) response is presented in the 200 hPa level, in addition to the 925 hPa and 500 hPa levels. The 925 hPa and the 500 hPa levels have been chosen represent the lower troposphere and mid troposphere responses, respectively. It should be noted that the 925 hPa levels is below than the surface over Antarctica, which in most places reaches up to 2000-3000 meters or roughly 650 hPa. The continental responses for the variables at this level has therefore been automatically estimated within SPEEDY using values from the lowest model level above the topography. The 200 hPa U response is shown to give an overview of the response close to the jet core. On the figures including a map of the SH, the 60^oS and the 30^oS latitude is marked with a red dashed line.

The annual mean and the JJA seasonal mean is shown for all variables. A comparison between the annual mean and the JJA mean indicates that the annual response is dominated by the differences between CTRL and EXP1 in the JJA season - the austral winter. As noted by Bromwich (1998), JJA is the season when the removal of sea ice creates the largest forcing.

The monthly mean GH and T response is also shown for March and September. These months are chosen for a more detailed description, as they represent two distinct states in the seasonal cycle of the model response.

5.2 Annual mean and winter mean response

5.2.1 Surface heat flux response

Figure 5.1 shows a map of the annual and the JJA seasonal response in surface heat flux (SHF). The surface heat flux includes both the sensible heat flux and the latent heat flux. Positive values indicate increased ocean-to-atmosphere heat flux, and negative values indicates decreased ocean-to-atmosphere heat flux.

In general, figure 5.1(a) shows a large increase in ocean-to-atmosphere heat flux over

areas where the sea ice has been removed in EXP1. The largest heat flux responses are located in the Weddel Sea and in the Ross Sea, both with maximums around 150 W/m^2. North of the ice edge present in the CTRL, located in a zonal band around 55 - 60^{o}S, there are areas with negative responses with maximum of about 40 W/m^2 in the south east of the Pacific sector, as seen in figure 5.1(a). Figure 5.1(b) shows that the major contribution to the annual mean response in SHF comes from the austral winter season. In this season, the increase in SHF over areas with sea ice removed has a maximum exceeding 250 W/m^2. The maximum decrease in SHF is around 100 W/m^2 and located over the same areas as in the annual mean.

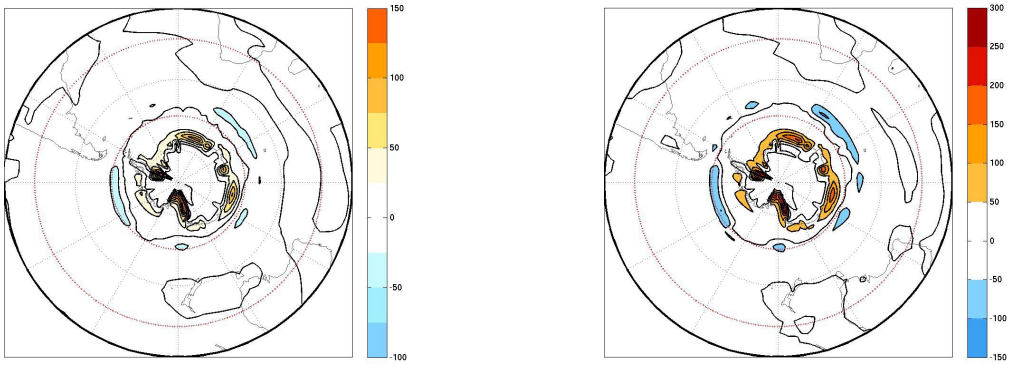

(a) Annual SHF response

(b) JJA seasonal SHF response

Figure 5.1: The surface heat flux response [W/m^2] for the annual mean(a) and the JJA seasonal mean (b). Positive values indicate increased ocean-to-atmosphere heat flux. The contour interval is 25 W/m^2 in the annual response (a) and 50 W/m^2 in JJA seasonal response (b). 60^{o}S and 30^o are marked with a red dashed line.

5.2.2 Temperature response

Figure 5.2 shows a large local increase in the lower tropospheric temperature over areas where the sea ice has been removed - especially concentrated around 60^{o}S. Figure 5.2(a) shows an increase of lower tropospheric temperature at 925 hPa with magnitudes between 10 - 15^{o}C in the Ross Sea, and between 10 - 15^{o}C in the Weddel Sea. The warming of the lower tropospheric air penetrates into the mid troposphere as shown in figure 5.2(b), but the magnitude of atmospheric warming decreases quickly with height. It is evident that the warming is more shallow in the Weddel Sea, than in the Ross sea and over the coast westward to Dronning Mauds Land. The maximum warming at 500 hPa is 2 - 3 ^{o}C over the coast in the western Ross Sea. In this layer, there are also negative (cooling) T responses around 50^{o}S with magnitudes between -0.5^{o}C and -1^{o}C (not visible in the figure). This creates a dipole response in the lower tropospheric T, with warming over the areas south of 60^{o}S, and cooling further north.

At the 925 hPa JJA seasonal mean (figure 5.2(c)), the same spatial pattern as in the annual mean is present, but with larger magnitudes (20 - 25^{o}C in the Ross Sea and 15 - 20 ^{o}C in the Weddel Sea). This is also evident at the 500 hPa layer (figure 5.2(d)). Here the maximum over the western part of the Ross Sea is between 3 - 4 ^{o}C. The cooling responses around 50^{o}S is also larger during the JJA season (-1 - -2^{o}C in the South Pacific) than in the annual mean. As in the annual T response, the warming is more shallow in the Weddel Sea, compared to the Ross sea and over the coast, westward to Dronning Mauds Land.

Figure 5.3 shows a zonal mean cross section of the annual mean T response in the SH. It is clear that the annual mean warming response is located south of 55^{o}S, with a maximum around 70^{o}S. The annual mean of the surface warming penetrates up to roughly 500 hPa in the troposphere. It is possible to see general spatial correspondence between the SHF responses shown in figure 5.1 and the large positive temperature responses near the Antarctic continent, but the negative anomalies in T are located farther north than the negative SHF anomalies. The equatorward displacement of the cooling response relative to the negative SHF response will be revisited in the discussion section.

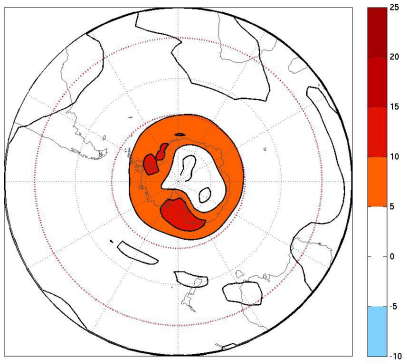

(a) Annual T response 925 hPa

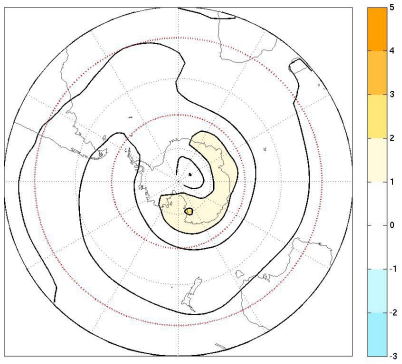

(b) Annual T response 500 hPa

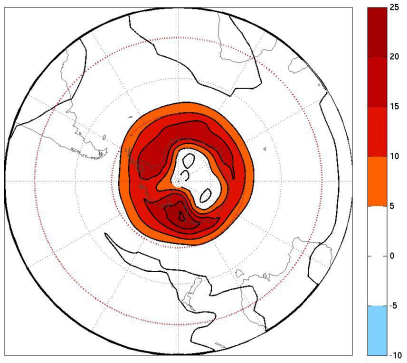

(c) JJA seasonal T response 925 hPa

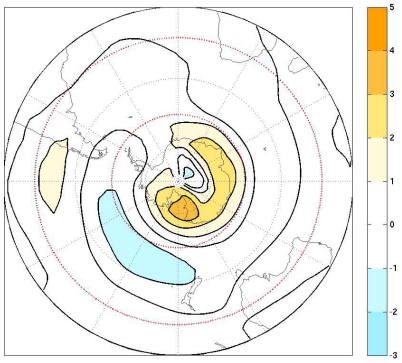

(d) JJA seasonal T response 500 hPa

Figure 5.2: The annual mean T response [^{o}C] at 925 hPa (a) and 500hPa (b). The JJA seasonal mean T response (^{o}C) at 925 hPa (c) and 500 hPa (d). Contour interval is 5 m/s for 925 hPa (a,c), and 1 m/s for 500 hPa (b,d). 60^{o}S and 30^o are marked with a red dashed line.

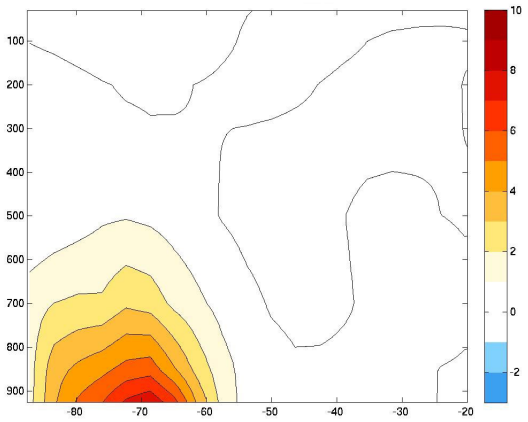

Figure 5.3: Latitude (x-axis) - pressure (y-axis) cross section of the annual and zonal mean temperature response [^oC]. The contour interval is 1^{o}C.

5.2.3 Geopotential height response

A positive GH response is evident over the areas with strong surface warming as seen in figure 5.4. The annual response at 925 hPa shown in figure 5.4(a) is positive over Antarctica and equatorward to 60 ^{o}S. The magnitude of the height increases at this pressure level are above 20 m, with magnitudes east of the Ross Sea reaching 60 - 80 m. Large positive responses are also found over Antarctica. Both Wilkes Land and Dronning Mauds Land exhibit positive GH responses of between 80 - 100 m, but these are suspect because they are estimated from the lowest model layer due to the topography. As with the SHF (figure 5.1), and T (figure 5.2), the dipole structure is present in the GH response. Over New Zealand and the South Pacific near 40^{o}S, responses of GH is negative with a magnitude of between roughly 20 and 40 m.

At 500 hPa, figure 5.4(b), the annual mean response is larger, but with roughly the same spatial pattern, consistent with the hypsometric equation 2.1. Over the Ross Sea there are positive responses of 120 - 140 m in magnitude. Two local maxima also appear at the coast of Dronning Mauds Land (100 - 120 m). The negative GH response located in the South Pacific is not significantly larger in amplitude than at 925 hPa, but the spatial area of the negative response GH is larger. Negative responses also appear in the southeast Indian Ocean at this level.

The austral winter response in GH is shown for 925 hPa in figure 5.4(c) and for 500 hPa in figure 5.4(d). The spatial patterns at both pressure levels are very similar to the annual mean response pattern. The magnitude of the austral winter response is generally larger than the annual mean response. East of the Ross Sea, the response is 80 -

100 m in magnitude at 925 hPa, while at 500 hPa the GH response is >180 m over this region. Over Antarctica at 925 hPa the maxima in GH increases are up to 140 m over Dronning Mauds Land and Wilkes Land. The coastal maxima over Dronning Mauds Land are present in 500 hPa with magnitudes greater than 180 m during JJA. The negative GH response magnitude is not qualitatively different in JJA, relative to the annual mean, but the horizontal extent of the response seems to be larger during the austral winter.

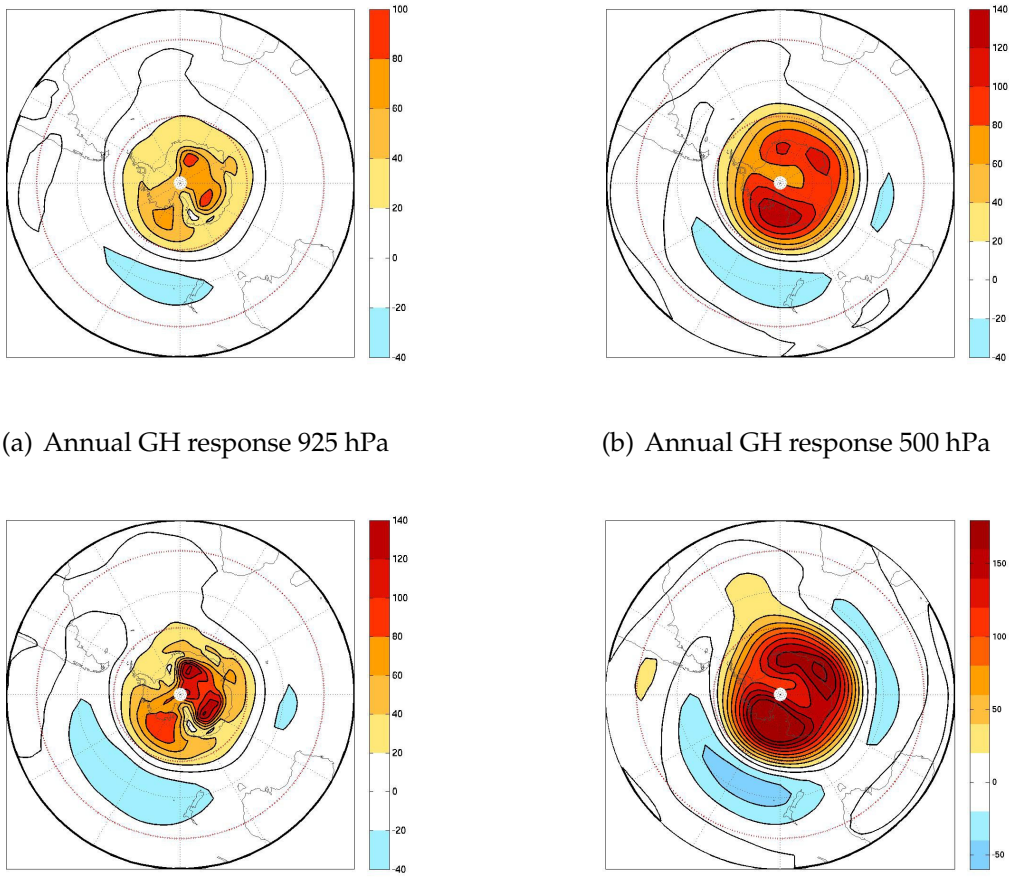

(a) Annual GH response 925 hPa

(b) Annual GH response 500 hPa

(c) JJA seasonal GH response 925 hPa

(d) JJA seasonal GH response 500 hPa

Figure 5.4: The annual mean GH response [m] at 925 hPa (a) and 500hPa (b). The JJA seasonal mean GH response (m) at 925 hPa (c) and 500 hPa (d). The contour interval is 20 m in each plot. 60^oS and 30^o are marked with a red dashed line.

Figure 5.5 shows a latitude-pressure cross section of the annual GH response in the SH. The response is positive everywhere poleward of 55^oS, with a maximum greater than 100 m between 500 - 100 hPa. From this figure, it is also evident that the zonal mean GH response at 925 hPa is between 40 - 60 m south of 70^oS and between 80 - 100 m for the same latitudes at 500 hPa. Comparing figure 5.5 with the cross section of the annual T response (figure 5.3) indicates an equivalent barotropic annual mean response

in the model, with positive GH anomalies and positive temperature responses at the surface. Positive anomalies in the isotherms follow positive anomalies in the isobars, and a equivalent barotropic state occurs as described in section 2.1. This response wil be revisited inthe discussion section.

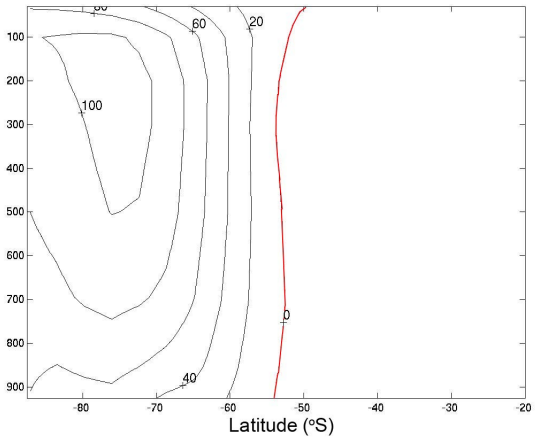

Figure 5.5: Latitude (x-axis) - pressure (y-axis) cross section of the annual mean geopotential height response [m]. The contour interval is 20 m and the 0 m contour line is marked red.

5.2.4 Zonal wind response

The annual and JJA seasonal mean response in U at 925, 500, 200 hPa is shown in figure 5.6 and figure 5.7, respectively. U is affected at all 3 levels. In general, there is a dipole response distributed in zonal structures in the SH. Around 60^{o}S, a decreasing U response occur in all layers. The positive responses are located around 40^{o}S and 80^{o}S.

Decreased zonal wind speeds in the annual mean at 925 hPa, shown in figure 5.6(a) have a maximum magnitude of 3 - 4 m/s, with maxima located over the South Pacific, north of the Ross Sea at 60^{o}S. Increased zonal wind speeds are located further north in the Pacific, and at the coast in the Ross Sea. These have magnitudes between 1 - 2 m/s. The spatial distribution of U anomalies is mainly concentrated to the Pacific sector at 925 hPa, but spreads out zonally aloft. At 500 hPa (5.6(b)), the largest decrease in U is in the South Pacific and has a magnitude of between 6 and 7 m/s. The positive responses are between 2 - 3 m/s around 40^{o}S in the Pacific, and between 3 - 4 m/s over the Ross Ice Shelf. The annual mean response at 200 hPa shown in figure 5.6(c) the negative responses located over the South Pacific has a magnitudes between -6 and -7 m/s. The positive responses, are located around 40^{o}S in the Pacific and over the Ross Sea and over the Ross Ice Shelf, with magnitudes between 3 - 4 m/s. In this layer the positive anomalies are covering larger areas than in the underlying layer. A zonal band of pos-

itive anomalies around 40^{o}S covers the whole South Pacific, the whole South Indian Ocean, and continues northwestward over the southern part of the Africa.

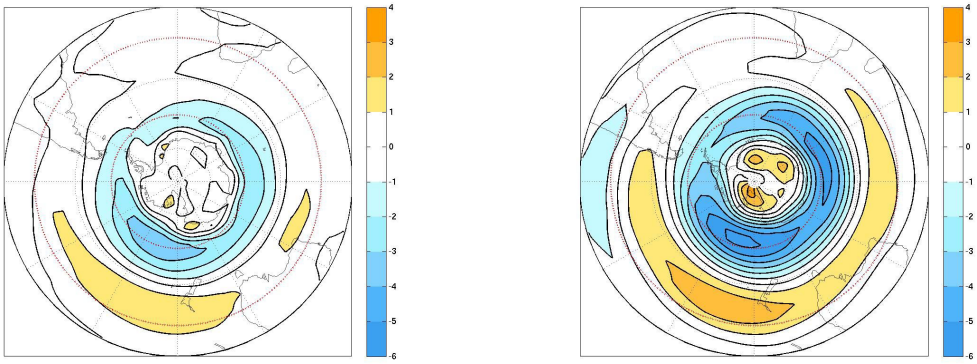

(a) Annual U response 925 hPa

(b) Annual U response 500 hPa

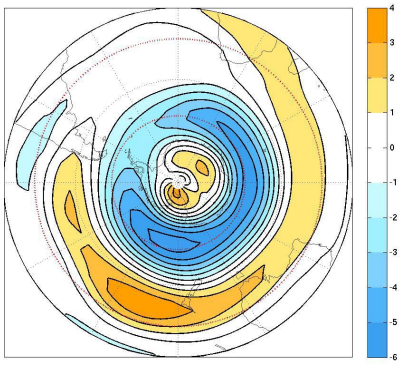

(c) Annual U response 200 hPa

Figure 5.6: Maps of the annual mean U [m/s] response. The response is shown at 925 hPa (a), 500 hPa (b), and 200 hPa (c). The contour interval is 1 m/s. 60^{o}S and 30^o are marked with a red dashed line.

By comparing the annual and the austral winter response, it is evident that most of the response is realized during the austral winter season. The spatial pattern of the annual response and the winter seasonal response is nearly the same. At 925 hPa, the maximum negative responses in U are between 4 - 6 m/s and the positive responses are between 2 - 4 m/s. The 500 hPa responses are between 10 - 12 m/s for the negative responses, and 2 - 4 m/s for the positive responses between 40 - 50^{o}S. Over the Ross Ice Shelf, the positive maximum responses in this layer are between 6 - 8 m/s. At 200 hPa, there are negative responses between 10 - 12 m/s and positive responses of 4 - 6 m/s around 40 - 50 ^{o}S, while the Antarctic coastal positive responses are reaching 6 - 8 m/s over the Ross Ice Shelf. It is evident that there is little amplification of the U response between 500 and 200 hPa.

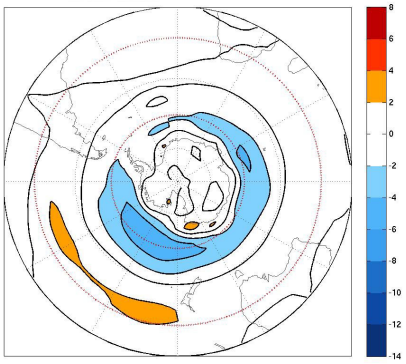

(a) JJA seasonal U response 925 hPa

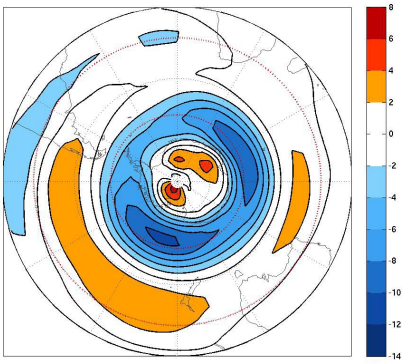

(b) JJA seasonal U response 500 hPa

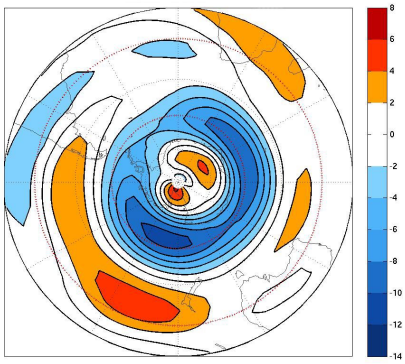

(c) JJA seasonal U response 200 hPa

Figure 5.7: Maps of the U [m/s] response for the JJA seasonal mean. The response is shown at 925 hPa (a), 500 hPa (b), and 200 hPa (c). The contour interval is 2 m/s. 60^oS and 30^o are marked with a red dashed line.

For a more detailed description of the differences in zonal wind between the CTRL run and the EXP1 run, figure 5.8 shows maps of the simulated austral winter seasonal mean U for the 925 hPa, 500 hPa and 200 hPa pressure levels. Different responses exists in the Pacific sector and in the Atlantic/Indian sector. The majority of the the Atlantic/Indian sector response seems to come from a decrease in the zonally averages flow, and this mainly affect the eddy-driven midlatitude jet at all levels. Within the Pacific sector, there seems to be a northward shift in the response with weakening of the eddy-driven jet around 60^oS, and with an extension in the jet westward from South America at 40^oS combined with an increase in the subtropical jet. This shift is most evident in the 925 hPa layer, but for the 500 hPa layer there is also increase in the zonal wind in EXP1 around 30^oS, while around 60^oS the jet in the Pacific seems to disappear. It is evident from the 500 hPa and the 200 hPa layers that the eddy-driven midlatitude jet is mainly affected at its maximum in the South Indian Ocean and in the Southwest Pacific, south of New Zealand. The structure of the subtropical jet is more or less the same in both

simulations.

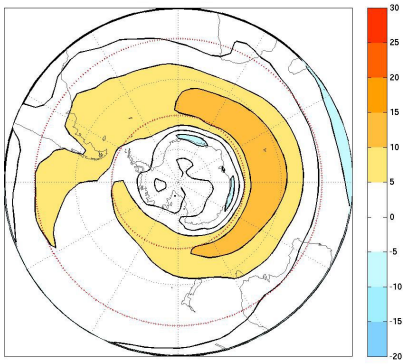

(a) JJA U 925 hPa CTRL

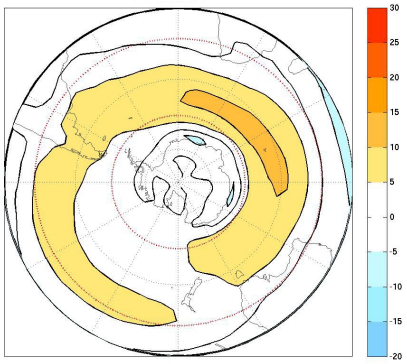

(b) JJA U 925 hPa EXP1

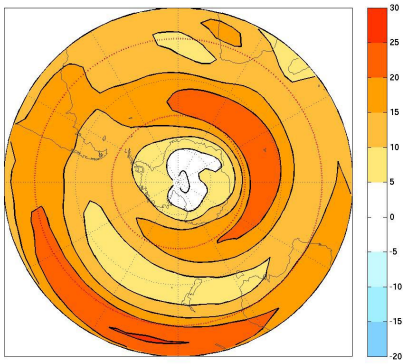

(c) JJA U 500 hPa CTRL

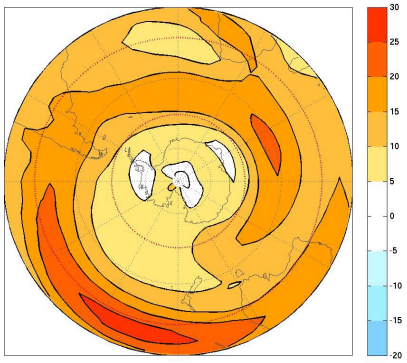

(d) JJA U 500 hPa EXP1

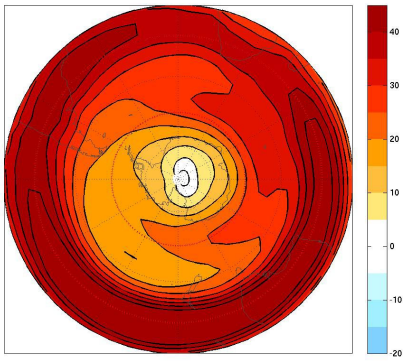

(e) JJA U 200 hPa CTRL

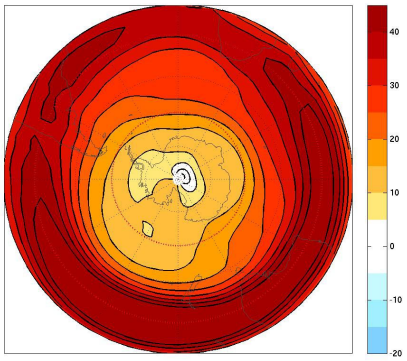

(f) JJA U 200 hPa EXP1

Figure 5.8: Maps of JJA seasonal mean U [m/s] at 925 hPa (a, b), 500 hPa (c, d), and 200 hPa (e, f). U are shown for the CTRL (left) and EXP1 (right) simulations. The contour interval is 5 m/s. 60^{o}S and 30^o are marked with a red dashed line.

The northward shift is evident in the latitude - pressure cross sections of the annual mean and the austral winter season mean zonal mean U shown in figure 5.9. This shift

in the jet could also be interpreted as a weakening in the eddy-driven midlatitude jet, with a weakened maximum between 600 - 400 hPa over 60 ^{o}S. The dipole structure in the response is clearly evident in both the annual and the austral winter seasonal means. There is a weakening and a northward shift in the zonal-mean mean U at all levels poleward of about 40^{o}S. By looking at figure 5.8 and 5.9 it is evident that the changes in the eddy-driven jet is largest during the austral winter season. The negative responses are much larger relative to the positive responses during the austral winter. The core in the subtropical jet at roughly 200 hPa is barely affected in either the annual mean or the austral winter mean.

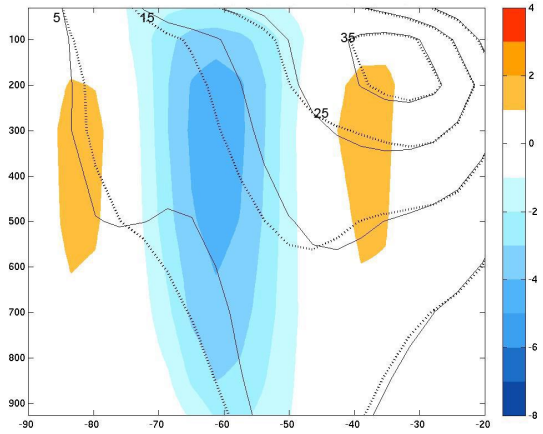

(a) Annual mean

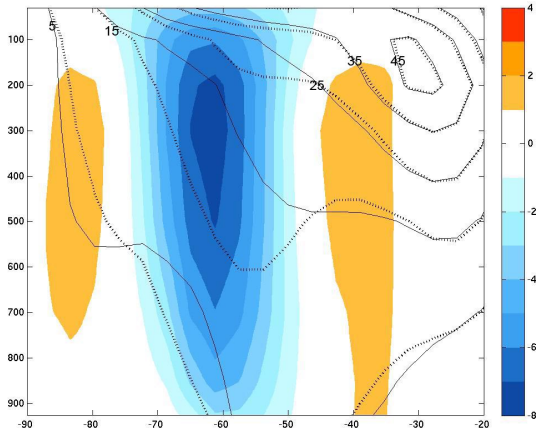

(b) JJA seasonal mean

Figure 5.9: Latitude (x-axis) - pressure (y-axis) cross section of the zonal mean U [m/s] response (colored background)[m/s]. The zonal-mean U from CTRL (dashed lines), and zonal-mean U from EXP1 (solid lines) simulations. The responses are shown for both the annual mean (a) and JJA seasonal mean (b). The contour interval for zonal-mean U climatologies are 10 m/s and 1 m/s in the response pattern.

5.3 T and GH response in September and March

As seen in the previous sections, the annual and austral winter seasonal responses display a consistent structural pattern with increased SHF from the ocean to the atmosphere, corresponding T increases, and positive GH responses, around the coast of the Antarctic continent. The winter response dominates the annual mean.

This section will evaluate the seasonal cycle of the response in more detail. Figure 5.11 shows the seasonal cycle of the monthly mean zonal mean maximum T and GH difference poleward of 60^oS at 925 hPa. The difference is obtained by subtracting the maximum zonal mean value at 925 hPa in EXP1, with the maximum zonal mean value at the same level in CTRL. Between mid April and mid November, during the extended austral winter, both responses are positive. The variability in the two responses also follows one another during these months, with a maxima in T and GH responses occurring in August. In the austral summer season (mid November, to the end of February) the T response is negative, with a minimum in January. The GH, however, has a positive response from mid November to mid February, and is negative from mid February to mid April. The GH response has a March minimum.

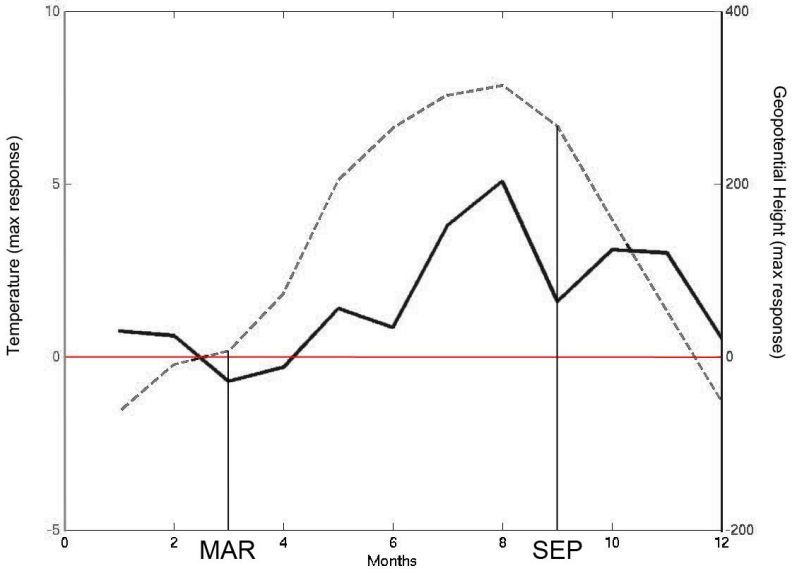

Figure 5.10: The seasonal variation of the maximum T response [^oC] (dashed) and the maximum zonal mean GH response [m] (solid) poleward of 60^oS. The left vertical axis is associated with the T values, and the right vertical axis is associated with the GH values. The x-axis is associated with the months.

Based on figure 5.11 and cross sections of monthly mean responses in T and GH (Appendix A.4), March (MAR) and September (SEP) are chosen for further investigation.

In MAR, the T response is positive with corresponding negative GH responses near the surface and positive GH responses aloft (figure 5.11) - an indication of a baroclinic response. To represent the atmospheric response indicating an equivalent barotropic response, typical of the majority of the monthly means and the annual mean, SEP has been chosen as it is 6 months removed from MAR and has a relatively large response. By comparing these two monthly means, it is possible to compare two distinct responses present in the model - the possible baroclinic response (MAR) and the equivalent barotropic response (SEP). The negative T response accompanied by a positive GH response found in the austral summer has been neglected from further consideration because the negative T response during this season could be an artifact of setting the SSTs to -1.5^{o}C in the locations where sea ice was removed. This is sometimes colder than the sea ice covered surface present in the CTRL. With a mild summer climate, the top layer of the sea ice could be covered with slush and water, which could be heated to a temperature above prescribed -1.5^{o}C in the EXP1 run.

Figure 5.11 shows a cross section of the monthly mean response in T and GH for SEP and MAR. The SEP responses in T and GH are dominated by a strong shallow warming at the surface (>10^{o}C) penetrating up to 400 hPa (figure 5.11(a), that is accompanied by a positive GH response throughout the whole troposphere (maxima greater than 180 m at 200 hPa) (figure 5.11(b)). In MAR, surface warming with magnitudes of 3^{o}C poleward of 70^{o}S (figure 5.11(c)) are associated with a deeper warming that penetrates up to 700 hPa. The GH response in MAR (figure 5.11(d)) is quite small relative to SEP (figure 5.11(b)) despite a small positive T response. The largest positive responses are found between 500 - 200 hPa (greater than 15 m). A negative response (more than -5 m) occurs near the surface below 850 hPa southward of 60 ^{o}S indicating a baroclinic response.

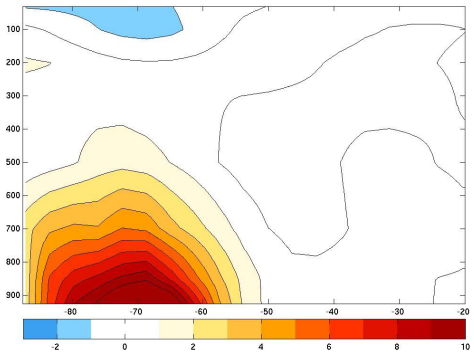

(a) Zonal mean T response SEP

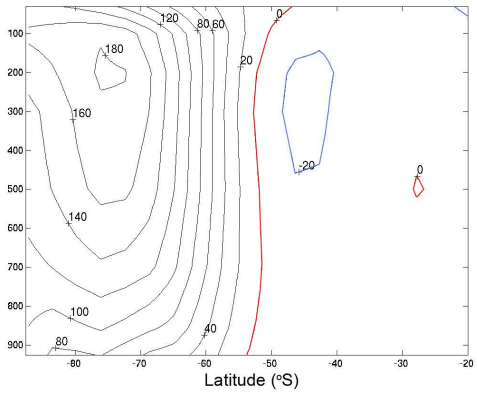

(b) Zonal mean GH response SEP

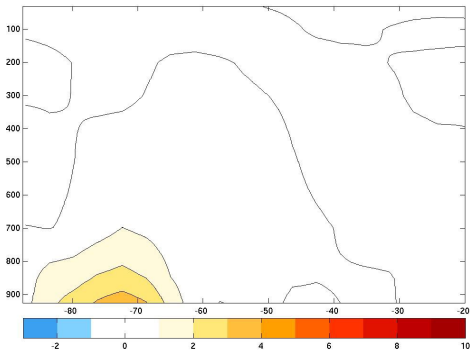

(c) Zonal mean T response MAR

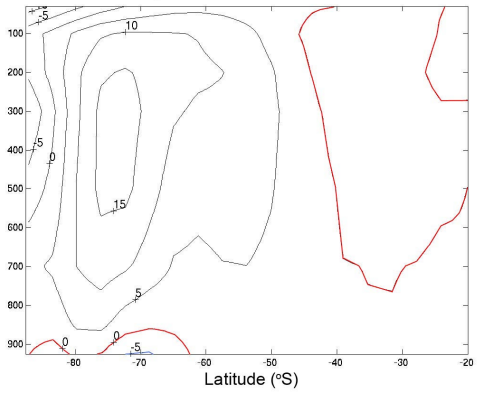

(d) Zonal mean GH response MAR

Figure 5.11: Latitude (x-axis)- pressure (y-axis) cross sections of monthly mean T response in September (a) and March (c) [^{o}C] and the monthly mean GH response in September (b) and March (d) [m]. For the GH response, the 0 m contour line is marked red while the negative values are marked blue. The contour interval for the T response is 2^{o}C for both months. The contour interval for the GH response is 20 m for September, and 5 m for March.

The spatial distribution of the temperature and geopotential height responses for the two months are shown in figure 5.12 and 5.13. ST follows the topography in the model, but since the SLP is the pressure at sea level, the SLP values over land are estimated using values of temperature and pressure at lowest model level above the topography. This is also the case for the 925 hPa responses over land, and should be taken into account when studying these areas.

In SEP, the ST response is positive, reaching magnitudes of over 35^{o}C in the Ross Sea and exceeding 30^{o}C in the Weddel Sea with a maximum over the Ronne Ice Shelf (figure 5.12(a)). The surface warming is most intense near the coast. There is a close agreement between the ST response and the 925 hPa T response (figure 5.12(c)), but the 925

hPa T response has smaller magnitudes. This is consistent with previous results that indicate that the warming decreases rapidly with decreasing pressure. The 925 hPa T response exceeds 22.5^{o}C in the Ross Sea, and reaches 17.5^{o}C in the Weddel Sea (figure 5.12(c)). The depth of the warming could be examined in figure 5.11, but the spatial distribution of the vertical T response is best seen in figure 5.12(e), which shows a map of the T response at 500 hPa. It is evident that the amplitude of T anomalies are much less at this altitude, with maxima located over the Ross Sea and at the coast of Enderby Land (east of Dronning Mauds Land). In the Ross Sea, the T response is between 2-3^{o}C, and is located right above the surface and lower tropospheric warming. In the Weddel Sea, there is no clear maxima in the T response corresponding to the maxima in the surface and lower tropospheric T response. This indicates a more shallow warming in this area. In stead, a maxima (2.5 - 3^{o}C) over Enderby Land occurs at this level. There are also areas with substantial cooling at this level. A zonal band of cooling responses is located between 45 - 50 ^{o}S, stretching from the South Pacific to the South Indian Ocean, with a maximum amplitude of -1.5 to -2^{o}C in the South Pacific. Cooling is also present at 500 hPa over central Antarctica (-1.5 - 2^{o}C).

The T response in MAR displays a much weaker response than in SEP. In the Ross Sea the ST warming has a magnitude around 20^{o}C, and in the Weddel Sea the warming is between 10 - 15^{o}C (figure 5.13(a)). Over the Ronne Ice Shelf, the ST warming exceeds 15^{o}C. The T response at 925 hPa follows closely the ST response, but with smaller magnitudes (7.5 - 10^o in the Ross Sea, and 5 - 7.5^{o}C in the Weddel Sea (figure 5.13(c)). The MAR T response at 500 hPa is more chaotic response (figure 5.13(e)). It is possible to see the connection between the 925 hPa T response and the 500 hPa T response in the Ross Sea, but it is shifted west at 500 hPa, with a maxima of 1.5 - 2^{o}C over Wilkes Land. There are also some smaller positive responses (0.5 - 1^{o}C) located at the coast of Dronning Mauds Land, in the Cosmonaut Sea, and north of Cooperation Sea. In this layer there are also signs of negative anomalies. These are located over the South Pole, over New Zealand and southwest Australia, and north of Marie Byrd Land.

The GH response in September has a vertical and spatial structure that follows the T response, especially aloft at 500 hPa. The SLP has a maximum in its response off the coast of Marie Byrds Land (5 - 7.5 hPa) (figure 5.12(b)). The large SLP response over Antarctica is estimated based on surface variables, as it is below the models topography. There are no notable responses in SLP within the Ross Sea and the Weddel Sea, which are the areas with the largest T responses at the surface and at 925 hPa. Negative SLP anomalies are found around 45^{o}S in the South Pacific and southwest of Australia. There are similarities between the SLP response pattern and the GH response at 925 hPa (figure 5.12(d)). The maxima over ocean are located at the coast of Marie Byrds Land (75 - 100 m). A larger response at 925 hPa GH response is found over Antarc-

tica, but for the same reason as the continental SLP values, these should be interpreted carefully as the 925 hPa level is located beneath the Antarctic continental surface. The GH response at 925 hPa has more spatial similarities with the surface and lower tropospheric T response than the SLP response.

As seen in the cross sections (e.g. figure 5.11(b)), the GH response has its maximum aloft. This is also evident in figure 5.12(f). Maxima in the GH response at 500 hPa are found over the Ross Sea (greater than 180 m) and over Enderby Land (greater than 180m). These maxima are located over the same areas as the maximum T response at 500 hPa, in general agreement with the surface and near ST responses. The negative responses in GH are also distributed over the same areas as the negative T responses in this layer.

The MAR SLP response is mostly negative (figure 5.13(b)). A band of negative anomalies between 2.5 - 5 hPa stretches along the coast from Wilkes Land eastward to the Weddel Sea. This negative SLP response is in contrast with the positive T anomalies at the surface during this month. The GH response in 925 hPa follows the same pattern with negative anomalies between 10 - 20 m (figure 5.13(d). Positive GH responses could be found over the Cosmonaut Sea (10 - 20 m). Positive GH response is also present at 500 hPa (20 - 30 m) (figure 5.13(f). East of Wilkes Land, there is a positive response at 500 hPa with a maximum amplitude of 40 - 45 m. This is located over the same area as parts of the negative GH response at 925 hPa. A qualitatively similar situation exists over the Weddel Sea, but here the magnitude in the positive GH response aloft is much weaker (10 - 20 m).

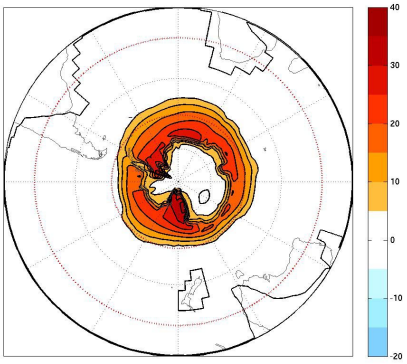

(a) ST response SEP

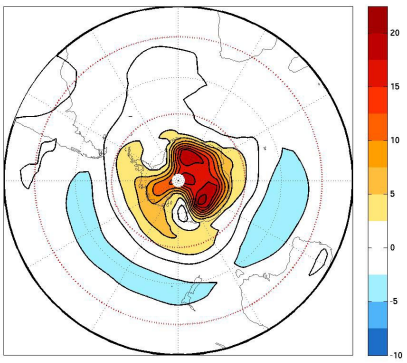

(b) MSLP response SEP

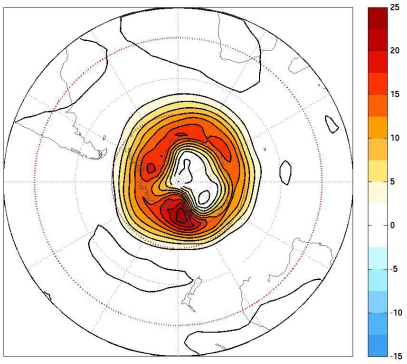

(c) T 925 hPa response SEP

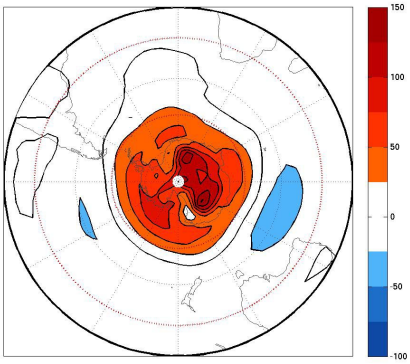

(d) GH 925 hPa response SEP

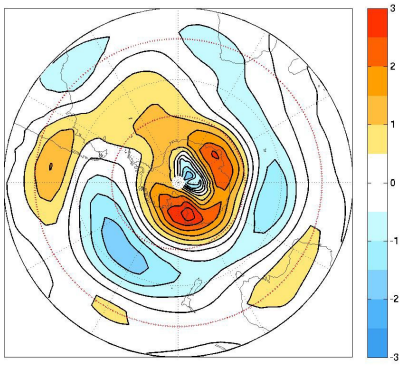

(e) T 500 hPa response SEP

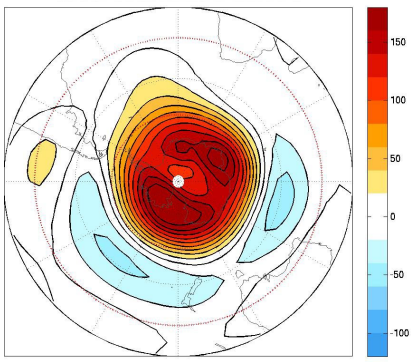

(f) GH 500 hPa response SEP

Figure 5.12: Monthly mean response maps for T [^{o}C] (left) and GH [m] (right) in September. The figure shows ST (a) and MSLP [hPa] (b), T (c) and GH (d) in 925 hPa, and T (e) and GH (f) in 500 hPa. Contour interval is 5^{o}C (a), 2.5^{o}C (c), and 0.5^{o}C (e) for T responses. The contour interval is 2.5 hPa(b), 25 m (d), and 20 m (f) for GH responses. 60^{o}S and 30^o are marked with a red dashed line.

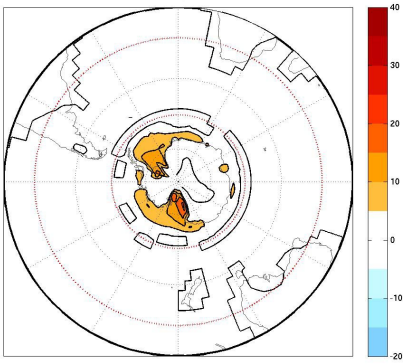

(a) ST response MAR

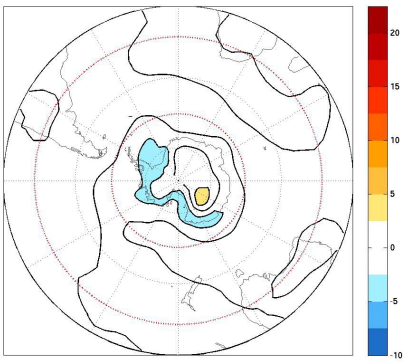

(b) MSLP response MAR

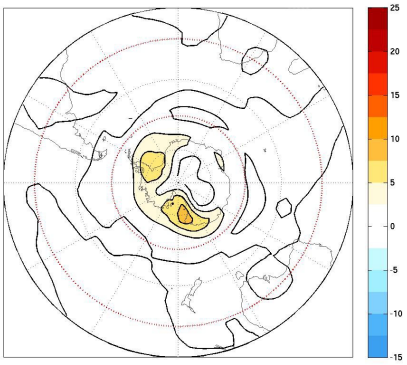

(c) T 925 hPa response MAR

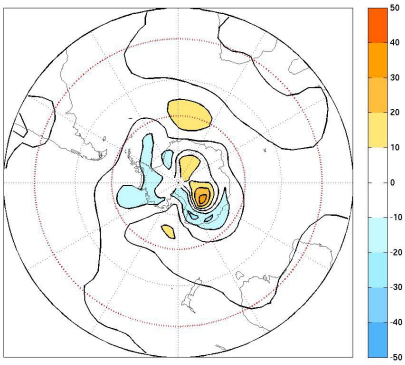

(d) GH 925 hPa response MAR

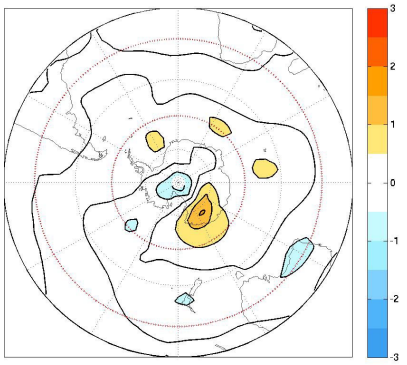

(e) T 500 hPa response MAR

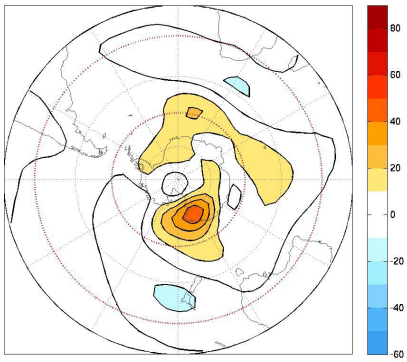

(f) GH 500 hPa response MAR

Figure 5.13: Monthly mean response maps for T [^{o}C] (left) and GH [m] (right) for March. The figure shows ST (a) and MSLP [hPa] (b), T (c) and GH (d) in 925 hPa, and T (e) and GH (f) in 500 hPa. Contour interval is 5^{o}C (a), 2.5^{o}C (c), and 0.5^{o}C (e) for T responses. The contour interval is 2.5 hPa (b), 10 m (d,f) for GH responses. 60^{o}S and 30^o are marked with a red dashed line.

5.3.1 Simulated GH responses versus hypsometric estimation

In this section, the simulated responses in GH at 500 hPa in MAR and SEP have been compared to an estimated response calculated from the hypsometric equation 2.1. ST from both the CTRL and EXP1 simulations has been used instead of T_v, and the surface pressure (SP) defines the reference pressure to estimate the maximum possible response due to the warming concentrated at the surface. The calculated CTRL values has been subtracted from the calculated EXP1 values to obtain an estimated 500 hPa GH response for both SEP and MAR.

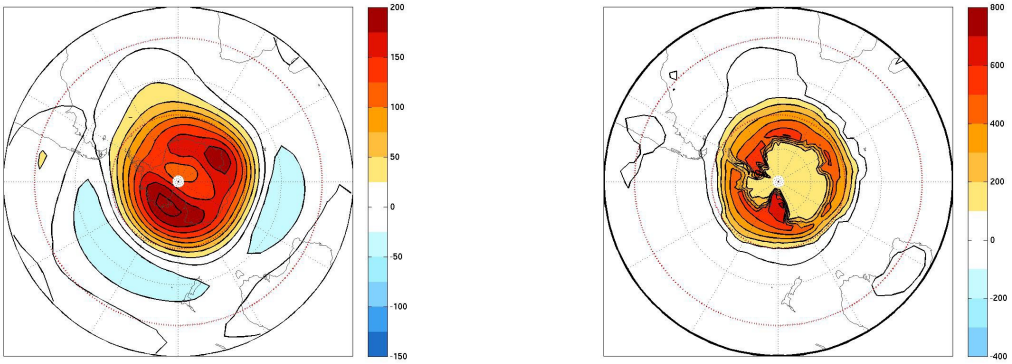

(a) Simulated GH response SEP

(b) Theoretical GH response SEP

(c) Simulated GH response MAR

(d) Theoretical GH response MAR

Figure 5.14: Simulated responses in GH [m] of 500 hPa for SEP (a) and MAR (c). The theoretical responses in GH of 500 hPa for SEP(b) and MAR (d). The contour interval is 25 m for a and b, and 100 m for b and d. 60^oS and 30^o are marked with a red dashed line.

Figure 5.14 shows the SPEEDY simulated GH response at 500 hPa for SEP and MAR (a and c), and the hypsometric-estimated GH responses at 500 hPa (b and d). In general, the hypsometric-estimated theoretical response is much larger and follows the spatial distribution of the surface warming exactly. This is as expected, because the hypso-

metric equation is a nne dimensional equation in the vertical, used here to estimate the GH anomalies directly above the SP and ST anomalies. In September, the estimated response (figure 5.14(b)) is about 3 times larger than the simulated response (figure 5.14(a)), with largest magnitudes in the Ross Sea (600 - 700 m) and in the Weddel Sea (500 - 600 m). In March, the estimated response (figure 5.14(d)) is up to 8 times larger than the simulated one (figure 5.14(c)) and appears at different locations. Negative estimated GH responses are not apparent in figure 5.14(b) and figure 5.14(d), although figure 5.12 and figure 5.13 shows negative anomalies in SP and ST. This is because the negative SP and ST responses are relatively weak compared with the positive ones.

The comparison between SPEEDY simulated and the hypsometric-estimated GH response at 500 hPa, gives an indication of the amount of local/non-local response within the SPEEDY simulations. The relative difference between the two GH responses is less in SEP than in MAR. In other words, the model simulated response in SEP is closer to the hypsometric-estimated response. The hypsometric-estimated response describes the maximum local response magnitude. This could indicate that the MAR response has a relatively larger non-local component in its response compared to SEP, consistent with the baroclinic response described previously.

5.4 Response in SH JJA seasonal variability

An EOF analysis has been performed to investigate the variability in the GH field during the JJA season. The 500 hPa level has been chosen to represent the EOFs for the CTRL and the EXP1 simulations as it allows to look at variability and mean change away from topography. This is also the level with largest mean GH change between the two model simulations. The EOF1 of 500 hPa GH field is a robust indicator of SAM as described in chapter 4.1.2 (Thompson & Wallace, 2000).

Figure 5.15 shows the EOF1 analysis for the GH at 500 hPa for CTRL, EXP1, and a merged matrix containing both model simulations. The spatial pattern of the EOF1 from CTRL is shown in figure 5.15(a) and from EXP1 in figure 5.15(b). The spatial patterns are similar in the two model simulations. The EOF1s are strongest in the eastern part of the Ross Sea and outside the coast of Marie Byrds Land. The difference in the EOF1s resulting from the two model simulations is not large spatially, but the magnitude of the maximum in the EOF1s is somewhat different. The EOF1 from both simulations seems to represent a SAM-like behavior. The maxima in the Ross Sea is larger in CTRL than in EXP1, but in EXP1, two smaller maxima appear over Wilkes Land and Dronning Mauds Land. There are also areas of negative values found in the two EOFs, but these are small relatively to the positive values. The distribution of the areas with negative values seems to be different in the two simulations. While the CTRL EOF1 displays a area of negative values the southern part of South America and in the South Indian Ocean, the negative values in the EOF1 from EXP1 are located in the South Pacific and in the South Indian Ocean.

An EOF analysis was also performed on a merged matrix containing 500 hPa GH data from both CTRL and EXP1 simulations. The EXP1 data has been appended to the end of the CTRL data. As a result a matrix with 100 time points is produced, with the first to fiftieth representing the CTRL simulation, and the fifty-first to one-hundredth representing the EXP1 simulation. The EOF1 for the merged matrix is shown in figure 5.15(c). This spatial pattern is most similar to the mean GH response at 500 hPa, but is also qualitatively similar to the EOFs based on the CTRL and EXP1 simulations separately. The primary temporal variability in the merged matrix is the shift in 500 hPa GH between the two data sets. This difference is seen in the PC1 of the merged matrix, as it is shifted after the 50 first data points (figure 5.15(d)). PC1 time series from the first 50 data points is highly correlated with PC1 from the CTRL and PC1 time series from second 50 is highly correlated with the PC from EXP1, so these two segments of combined analysis represent SAM-like variability in the CTRL and EXP1, respectively. Conclusion from the merged analysis is that largest difference in PC1 time series is a shift in the mean 500 hPa GH, which is consistent with similarity of EOF1 merged and

difference between CTRL and EXP1. Difference in SAM-like behavior are less obvious from merged analysis.

By looking at time series of the PC1 there are no obvious differences between the internal variance of the first half (EOF1 CTRL) and the second half(EOF1 EXP1). Therefore the standard deviation in the CRTL half and the EXP1 half of the PC1 has been calculated individually. By this calculation, it is evident that the variance in the EOF1 is less in the GH of EXP1 at 500 hPa (σ=0.3681), compared to the CTRL (σ=0.4031). This is also the conclusion drawn based on the raw variance associated with the first PCs corresponding to the separately EOF1s from CTRL and EXP1 simulations (not shown).

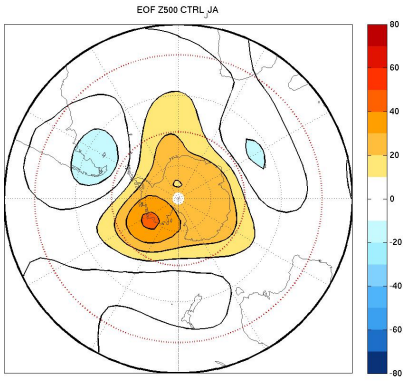

(a) EOF1 500 hPa CTRL

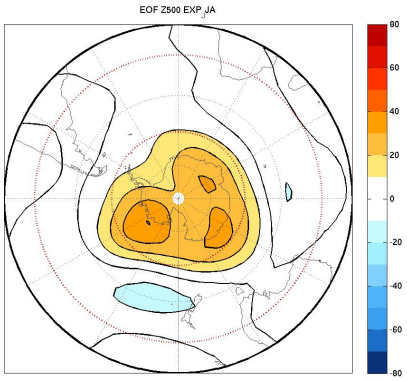

(b) EOF1 500 hPa EXP

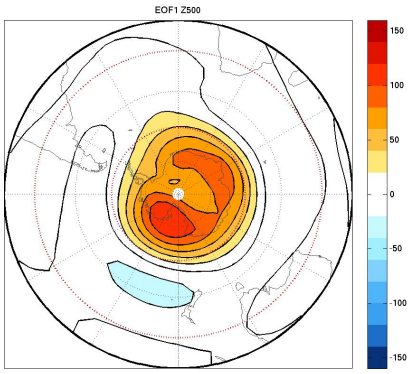

(c) EOF1 500 hPa CTRL-EXP1 merged

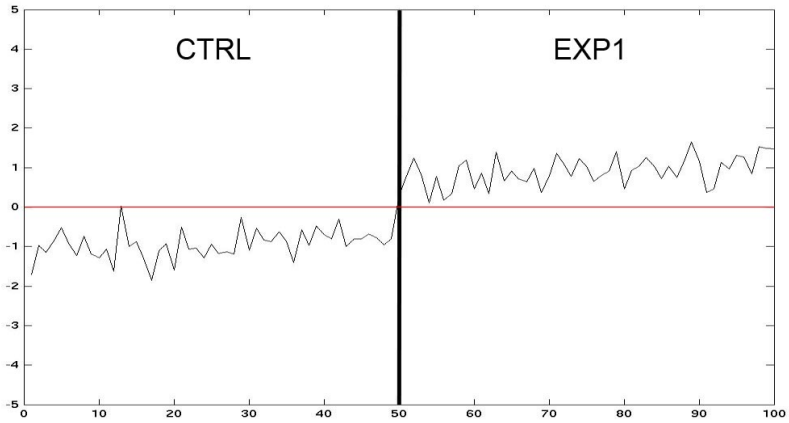

(d) PC1 500 hPa CTRL-EXP1 merged

Figure 5.15: EOF1 of 500 hPa GH from EXP1 (a) and CTRL (b) simulations separately, and a merged matrix containing both simulations (c). The first PC for EOF1 of the merged matrix is show in d. The contour interval is 10 m for the individual EOF1s, and 20 m for the merged EOF1. 60^{o}S and 30^{o} are marked with a red dashed line.

Chapter 6

Discussion and conclusion

6.1 Introduction

By performing two model simulations, the atmospheric response to year round open water in the southern hemisphere (SH) has been investigated. A control run (CTRL) with a seasonal cycle based on climatology from the ERA-15 dataset has been performed, in addition to an experimental run (EXP1) where areas covered with sea ice have been replaced with fixed SSTs of -1.5^{0}C.

The model simulations indicate that sea ice removal is followed by a strong local surface warming at the surface around the Antarctic continent. With no sea ice present, the warming in the near-coastal surface temperature around Antarctica is at its largest during the austral winter season. As shown in figure 5.1, the surface heat flux increases over areas with removed sea ice in the annual mean, but the annual response is dominated by the austral winter season. Considering the amplitude of the responses, a dominant austral winter season response is prominent for all the variables studied in this thesis. This is in agreement with findings in Bromwich (1998). During the austral summer season, the response in surface and near-surface temperature is slightly negative. A reason for this may be the fact that the fixed SSTs used to replace the sea ice covered areas is colder that the surrounding SSTs, and therefore causing negative and probably artificial anomalies in the response. Local SH responses found during the austral summer are therefore excluded from further considerations. Negative thermal responses could also affect the pre-winter season (March and April). March and April are the months where the zonal circulation in the SH is at its weakest and the the positive thermal forcing is not yet dominant.

The strong local thermal response is associated with a GH response. This response is mainly positive throughout the troposphere, creating an equivalent barotropic response to the surface warming. This is the general pattern of the monthly response in the austral winter season, where the T anomalies are positive. Deviations from this response pattern are found in the austral summer (as mentioned, negative temperature responses and positive geopotential height responses) and in March (weak positive temperature response, areas of negative geopotential height responses near the surface and positive geopotential height responses aloft indicating a baroclinic response).

6.2 Annual and austral winter response

6.2.1 Surface heat flux response

The responses in SHF is strongly positive over areas where the sea ice has been removed. This is as expected from previous experiment such as Flugge (2009) and

Bromwich (1998). With the sea ice removed, the insulating effect of the ice is no longer present and heat exchange between the ocean surface and the lower atmospheric layer is allowed. Since the fixed SST of -1.5^{o}C used to replace the sea ice is substantially warmer than the near surface air, the heat flux from the ocean to the atmosphere will increase. The heat flux includes both sensible and latent heat release.

North of the former ice edge, areas of negative surface heat flux responses are found. The cooling responses could be explained in two ways. The first explanation is that the local decreases in near surface wind results in decreased turbulence close to the surface. The interaction between the surface stress and the surface temperature could be described by equation 6.1.The surface layer potential temperature (θ_*^{SL}) , the vertical kinematic potential temperature flux at the surface ($w'\theta'_S$), and the friction velocity (u_*) is tied together in equation 6.1 using theory from Reynold stress as described in Stull (1989).

$$\theta_*^{SL} = \frac{-\overline{w'\theta'_S}}{u_*} \tag{6.1}$$

The second explanation is that advection of cold air from over the sea ice to over the warm ocean water no longer occurs at the equatorward extent of sea ice in the CTRL simulation, but rather occurs at the Antarctic coast. This is a process that causes a positive ocean-to-atmosphere heat flux. With the sea ice edge no longer present in the EXP1 run, the temperature difference between the ocean and the atmosphere at the equatorward extent of the CTRL sea ice distribution would be relatively smaller, thus resulting in an negative surface heat flux response.

6.2.2 Temperature response

The temperature response follows closely the surface heat flux response. Areas with removed sea ice experience strong shallow warming, with increased heat flux warming the overlaying air. The response strongly resembles the findings in Flugge (2009) and Bromwich (1998). Transfer of sensible heat, diffusion and release of latent heat due to convection increases the penetration of the warming. The surface warming will also change the meridional temperature gradient at the surface, up to the highest level affected by the heat source. As the SH meridional temperature gradient is associated with colder air towards the pole, such warming will weaken the meridional temperature gradient over the Southern Ocean, especially near where the sea ice has been removed. The area with the strongest meridional temperature gradient, which was located at the former ice edge, will move towards the coast of Antarctica when the sea ice is removed.

The negative temperature responses around 50^oS in the South Pacific could been seen in connection with the geopotential height response. This will be discussed in the next section.

6.2.3 Geopotential height response

The shallow penetration of the surface warming, is associated with a change in the overlying geopotential height. The relationship between temperature and the geopotential height is described in the hypsometric equation 2.1. Increasing the temperature between two pressure levels Z_1 and Z_2 will increase the height between the two, thus the geopotential height difference is given by $h = Z_2 - Z_1$. The dipole structure of the geopotential height response could be explained by the decrease in the meridional temperature gradient in the SH. This will increase the geopotential height over the polar areas of the SH, and decrease the geopotential height over the southern oceans as seen in figure 5.4 due to shifting of atmospheric mass. The areas with decreased geopotential height are coupled with the areas of decreased temperature seen in figure 5.2. As a result of the increase in geopotential height near the pole and decrease in geopotential height over southern oceans, the meridional pressure gradient in the SH will be weaker.

In the annual mean and in the JJA seasonal mean, the atmospheric GH response is equivalent barotropic. Over all areas with surface warming present, the GH increases both at 925 hPa and 500 hPa. The largest increase in GH is aloft, between 500 - 100 hPa as seen in figure 5.2.3. The general decrease in SLP found in Bromwich (1998), is not present in this experiment. In Flugge (2009) only September showed an similar atmospheric response. An equivalent barotropic response can be associated with a dominant non-linear secondary circulation or as an immediate local geopotential height response to the surface warming. The dominating processes required to get an equivalent barotropic response are discussed in section 6.3.

6.2.4 Zonal wind response

The annual and austral winter zonal wind response is dominated by a dipole structure, as seen in figure 5.6. Such a dipole response is also evident in Bromwich (1998) and in Flugge (2009). The annual mean austral winter mean zonal wind responses could be described by the thermal wind relationship 2.3. With the equivalent barotropic response, present in the austral winter seasonal mean and in the annual mean, follows a decrease in the meridional horizontal T gradient over the southern oceans, in addition to a decreased meridional horizontal pressure gradient. This response changes the magnitude of the geostrophic wind at each affected level by changing the balance be-

tween the Coriolis force and the pressure force. In an equivalent barotropic situation, the geostrophic wind is allowed to change with height, creating a vertical shear, but the direction between the low level and upper level geostrophic wind is parallel. The thermal wind in an equivalent barotropic situation therefore changes only the magnitude, not the direction of the geostrophic wind.

The main response in the zonal-mean zonal wind is associated primarily with a weakening, but also a northward shift of the eddy-driven midlatitude jet, which extends all the way down to the surface. A northward shift helps to explain the dipole structure in the zonal wind response. This is seen in figure 5.9, where the zonal mean structure for both the CTRL and EXP1 is shown in addition to the zonal mean response pattern. The meridional shift is most evident in the Pacific sector, while the weakening of the mean flow is most characteristic in the Indian Ocean sector. A weakened eddy-driven midlatitude jet could also be associated with changes in the SH storm tracks as this jet is central in the transport of momentum polewards from the subtropical jet. Studies with reduced sea ice in the Arctic region shows a locally reduced storminess in the boreal winter season (December, January, and February) (Seierstad & Bader, 2009), and in the similar experiment for the SH, Flugge (2009) suggested less storm activity poleward of 60^oS between May and October. The subtropical jet is barely affected.

6.3 MAR and SEP atmospheric response

6.3.1 Linear or non-linear adjustment

Two characteristic atmospheric responses are present in the model results - the equivalent barotropic and the baroclinic state. The austral winter season has a equivalent barotropic response pattern. A meridional temperature gradient is present, but the thickness and the height contours are parallel due to the overall positive geopotential height response over the surface warming. This situation is prominent for the annual response except in the austral summer (negative T responses) and March. During March, the zonal mean geopotential height response is weak baroclinic, with a small negative response found at the surface around 75^oS. The magnitude of the zonal mean of this monthly mean decreased geopotential height is about -5 m (figure 5.11). This baroclinic structure is evident in the spatial distribution of the GH anomalies as seen in figure 5.13, with strongest structural pattern in the western part of the Ross Sea.

Two qualitatively different atmospheric responses are described in the equivalent barotropic and baroclinic responses. The baroclinic response could be seen as the first order atmospheric response with linear processes dominating the circulation pattern. The warming of air masses induces convective motion. The continuity equation A.3 is valid for

air masses. With rising motion creating decreasing geopotential height at the surface (surface low) and a shortfall of air, this has to be compensated with horizontal advection of mass. This leads to a convergence zone at the surface and a divergence zone with increased geopotential height aloft. Such a circulation could also be described by the thermodynamic energy equation (equation 2.11). By this, it is seen that the warming must be compensated by horizontal temperature advection given by $\overline{u}\frac{\partial\theta'}{\partial x}$ and $v'\frac{\partial\overline{\theta}}{\partial y}$. With $\frac{\partial\overline{\theta}}{\partial y} < 0$, equatorward motion is induced, v'>0, and implying a surface low east of the surface warming according to quasi-geostrophic theory Hoskins & Karoly (1981). The equivalent barotropic response could be seen as an immediate local atmospheric response to the surface warming or as a result of non-linear secondary circulation reversing the circulation associated with a linear baroclinic response, as described in section 2.1 (figure 2.4). With a secondary non-linear circulation dominating over the primary linear circulation, the baroclinic atmospheric response is disappearing in favor to the equivalent barotropic atmospheric response. The circulation pattern connected to linear baroclinic response is reversed. Divergent eddy vorticity flux and converging air mass is found aloft. At the surface, divergence of air mass and ridging occurs. Such secondary circulation can be explained by studying the terms in the quasigeostrophic vorticity equation 2.10. Induced vorticity from the meridional advection, $\beta v' > 0$, causes descending of air. In the absence of advection of relative vorticity, the induced divergent vorticity anomaly must be balanced by $\frac{\partial\omega}{\partial p} < 0$. ω' increases with decreasing pressure, and indicate descending motion accompanying increased pressure with time as $\omega' = \frac{Dp}{Dt} > 0$ Fagerli (2008). The omega equation 2.12, which includes both the thermodynamic equation and the vorticity equation, can be used to estimate ω.

The seasonal cycle of the geopotential height and temperature response in the model is seen in figure 5.3. The development of the relationship between the temperature response at the surface and the geopotential height response aloft can be studied. The temperature response has a strong seasonal signature with slight cooling at the surface during the austral summer season, and strong surface warming in the extended austral winter. March is the first month after the austral summer when the surface warming is present. This sets off the first order circulation and creates a baroclinic geopotential height response. By studies of cross sections of monthly mean responses, the development of the temperature and geopotential height responses has been investigated (Appendix A.4). From April and into the austral winter season, the thermal forcing becomes gradually stronger and the geopotential height response develops into a equivalent barotropic response. This could be interpret as a more local immediate equivalent barotropic response or an increased secondary circulation from April into the austral winter, with a strong non-linear character. It could also indicate that the non-linear circulation takes time to develop, or that it requires a certain amount of thermal forcing to be initiated.

6.3.2 Local or non-local response

The removal of sea ice can induce both local and non-local responses. Local responses can be identified as the surface warming or the geopotential height anomalies present above the surface warming. To which amount thermal anomalies can induce a large scale atmospheric response, depends on the ability to produce Rossby Waves (Holton, 2004). The comparison between the hypsometric-estimated response in geopotential height at 500 hPa and the SPEEDY simulated geopotential height response at the same level, revealed large differences between the two. The deviations were also larger in March than in September. This probably indicate an immediate local equivalent barotropic response to surface restricted warming, in addition to the non-linear component of the response.

The hypsometric-estimated response was calculated using the hypsometric equation 2.1. As this calculation only estimates a geopotential height response based on the surface anomalies in temperature and pressure, it represents the largest local response possible. By studying the ratio between hypsometric-estimated response and SPEEDY simulated response, the extent local versus non-local geopotential height response can be qualitatively addressed. In March, the hypsometric-estimated response in geopotential height at 500 hPa is 8 times larger than the SPEEDY simulated response. The September hypsometric-estimated response is 3 times larger than the SPEEDY simulated one. This could indicate a more non-local response pattern in March than in September consistent with the baroclinic response. It also implies that the induction of an equivalent barotropic response in September has a strong local component, in addition to non-linear secondary circulation. Another argument for the influence of atmospheric dynamics is that while the estimated response is restricted only to areas with surface anomalies, the simulated responses are smoothed out exceeding the spatial coverage of the surface anomalies. This smoothing seems to be most prominent during March.

An explanation of the more non-local response in MAR could be that the zonal wind is baerly affected in MAR (figure 6.1). The zonal wind in March is weaker than in September, but in September there is a reduction in the eddy-driven midlatitude jet. The shift of the jet in EXP1 is also different in the two months, with a equatorward shift present in September and a slight poleward shift in March. This jet is important in the process of transporting momentum polewards from the subtropical jet and in the general interaction between polar regions and midlatitudes. With a weaker eddy-driven jet in EXP1 during September this interaction could be affected.

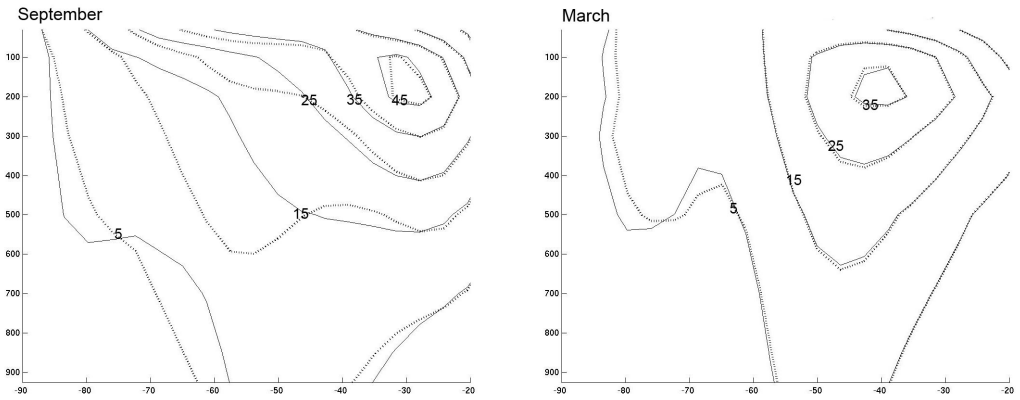

Figure 6.1: Latitude-height cross sections of the zonal mean monthly mean zonal wind for CTRL (dashed) and EXP1 (solid) in September (left) and March (right). The contour interval is 10 m/s.

6.4 Response in SH JJA seasonal variability

The geopotential height variability at 500 hPa during austral winter season has been studied by performing an EOF analysis on the seasonal mean from both the CTRL and EXP1 simulations. The first EOF, EOF1, representing the Southern annular mode (SAM), is associated with a spatial variability pattern that is similar in both the CTRL and EXP1. The difference between the two is the magnitude of the variability, as this is larger in the CTRL EOF1 than in the EXP1 EOF1. The first PC, PC1, from each individual model simulation reveal a larger variability in the time series from the CTRL simulation. As the EOF1 represents SAM in the two model simulations, this could indicate a less active SAM in EXP1. With a strong surface warming around the coast of Antarctica and a corresponding increase in geopotential height aloft due to the equivalent barotropic response in this season, the eddy driven midlatitude jet is decreasing in strength. The jet has an important influence on the variability of the polar regions, and a decrease in its magnitude could be connected to the less active SAM in the EXP1. In EXP1 the strong surface warming associated with the former sea ice edge, is moved towards the Antarctic coast. This may move the baroclinic zones south of the active latitudes of the storm tracks. The storm track and the eddy-driven midlatitude jet may consequently be weaker. To the extent that the SAM could be associated with fluctuations in the eddy-driven midlatitude jet, a weaker SAM may be consistent with a weaker storm track and sea ice loss in the SH. Reduction in storminess is found in similar experiments for SH (Flugge, 2009) and for the NH Seierstad & Bader (2009).

The spatial variability pattern from the first EOF resulting from an analysis of the merged CTRL and EXP1 simulations, is similar to the mean annual and mean austral

winter difference in geopotential height at 500 hPa between the two model simulations. The majority of the variance in the whole PC1 time series results from the shift after the 50 first data points, which is associated with the mean change between the two model simulations. Qualitatively this mean change represents increased geopotential height over the Antarctic region and a weaker eddy-driven midlatitude jet, which is also commonly associated with the SAM. In the negative SAM phase the eddy-driven midlatitude jet is absent in the Pacific sector Codron (2007). This could also be seen in the austral winter mean of zonal wind (figure 5.8) for the EXP1 simulation. Also seen in this figure is the stronger subtropical jet in the Pacific sector, which also is associated with a SAM. Flugge (2009) studied the correlation between the geopotential height response at 500 hPa and SAM. He found that the largest correlation in September, where the geopotential height and temperature response was roughly similar to an equivalent barotropic response.

6.5 Further Work

The analysis of the CTRL and EXP1 has revealed some characteristics of an atmospheric response to sea ice removal in SH. The model set up for the EXP1 simulation, with fixed SSTs of -1.5^{o}C replacing the sea ice in the SH, is maximizing the amplitude of the response drastically by eliminating SH sea ice , even in winter. This is similar to the experiment done by Bromwich (1998). The responses in the austral summer has been neglected, as they may be a result of the unrealistic nature of the fixed SSTs. During this season the model projects negative surface heat flux and temperature responses. Probably because the fixed SSTs are colder than the near surface air. Instead of fixed SSTs, it is suggested that projected SSTs including a seasonal cycle would produce a more realistic response.

Removing sea ice effect the zonal wind. The main response includes a dipole structure with a weaker eddy-driven midlatitude jet. As this jet is of great importance in the interaction between the polar regions and the midlatitudes, the impact of a reduced eddy-driven midlatitude jet can be studied. Such a study could also involve the connection between the jet and SAM, as the EOF analysis performed in this thesis indicates a less active SAM shifted towards its negative phase in EXP1, compared to CTRL. Such a study could be accompanied by a more detailed variability study of SEP and MAR, as they represent the two different atmospheric responses - equivalent barotropic and baroclinic, respectively. As seen in figure 6.3.2, the zonal wind in March is slightly shifted polewards, and the zonal wind in September is shifted equatorwards. These shifts in zonal wind are commonly associated with positive/negative SAM, respectively (Codron, 2007).

The amount that the responses to SH sea ice removal are local or non-local is briefly studied in this thesis. Results indicates a more non-local response in the baroclinic state of March relatively to the equivalent barotropic state in September. By this, the amount of local adjustment compared to non-linear secondary circulation adjustment in the September geopotential height response can be investigated. The influence on the northern hemisphere (NH) was mentioned by Bromwich (1998). In the Bromwich-experiments it was shown that wave anomalies induced by sea ice removal in the SH, could propagate into the NH on a timescale of month. Studies of latitude-height cross sections showing the monthly zonal mean response of geopotential height (Appendix A.4), indicates anomalies over the Arctic regions during the boreal winter.

Appendix A

Basic equations and derivations

A.1 The primitive equations

This section gives an overview of the primitve equations that describes the atmosphere. To simplyfiy the equations, in meteorology it is common to refer to pressure coordinates, rather than carthesian coordinates (Holton, 2004). The equations and the different derivations can be found in Holton (2004). The equations are shown in both carthesian coordinates (left side) and pressure coordinates(right side).

The horizontal momentum equation

$$\frac{D\mathbf{V}}{Dt} + f\mathbf{k} \times \mathbf{V} = -\frac{1}{p}\nabla p \Leftrightarrow \frac{D\mathbf{V}}{Dt} + f\mathbf{k} \times \mathbf{V} = -\nabla\phi \tag{A.1}$$

The hydrostatic equation

$$\frac{\partial p}{\partial z} = \frac{p}{RT}g = -\rho g \Leftrightarrow \frac{\partial \phi}{\partial p} = -\alpha = -\frac{RT}{p} \tag{A.2}$$

The continuity equation

$$\frac{1}{\rho}\frac{D\rho}{Dt} + (\nabla \bullet \mathbf{V})_H = 0 \Leftrightarrow (\nabla \bullet \mathbf{V})_p + \frac{\partial \omega}{\partial p} = 0 \tag{A.3}$$

The thermodynamic energy equation

$$c_p\frac{DT}{Dt} - \alpha\frac{Dp}{Dt} = J \Leftrightarrow (\frac{\partial}{\partial t} + \nabla \bullet \mathbf{V})_p T - S_p\omega = \frac{J}{c_p} \tag{A.4}$$

$\mathbf{V}$ is the horizontal velocity vector, t is time, $f = 2\Omega sin\phi$ is the Coriolis parameter, p the pressure, Φ the geopotential height, z the Cartesian height, ρ is the density of air, $R = 287\frac{J}{kgK}$ the gas constant for dry air, c_p the specific heat for dry air at constant pressure, J the rate of heating per unit mass, $S_p = -\frac{T}{\Theta}\frac{\partial \Theta}{\partial p}$ is the static stability parameter for the isobaric system and $\omega = \frac{Dp}{Dt}$ the rate of change in pressure following the motion.

The transcription between Cartesian coordiantes and pressure coordinates follows

$$\frac{D}{Dt} \equiv \frac{\partial}{\partial t} + \left(u\frac{\partial}{\partial x} + v\frac{\partial}{\partial y} + w\frac{\partial}{\partial z} \right) \Leftrightarrow \frac{D}{Dt} \equiv \frac{\partial}{\partial t} + \left(u\frac{\partial}{\partial x} + v\frac{\partial}{\partial y} \right) + \omega\frac{\partial}{\partial p} \tag{A.5}$$

A.2 Derivation of linear response to surface heating

Equation 2.2 is derived as shown in this section. This derivation is also shown in Fagerli (2008); Flugge (2009). The derivation starts of with the hydrostatic equation integrated in the vertical direction.

$$Z_{500} = \frac{R < T >}{g} ln\left(\frac{p}{500}\right) \tag{A.6}$$

It is then assumed that the temperature could be divided into a mean state and a perturbed state.

$$< T >= \overline{T}_a + T_0' \tag{A.7}$$

and

$$p = p_0 + p'_{surface} \tag{A.8}$$

Here p_0=1000,$\overline{T}_a$ is the mean atmospheric temperature, T_0' is the imposed midlatitude SST, and $p'_{surface}$ is the surface pressure anomaly. It should be noted that the SST anomaly allows the entire lower half of the troposphere to come into thermal equilibruiium (Fagerli, 2008), Kushnir *et al.* (2002). This means that equation A.6 could be written as

$$Z_{500} = \frac{R(\overline{T}_a + T_0')}{g} ln\left(\frac{1000 + p'_{surface}}{500}\right) \tag{A.9}$$

$$Z_{500} = \frac{R(\overline{T}_a + T_0')}{g} ln\left(\frac{1000 + p'_{surface}}{1000}\frac{1000}{500}\right) \tag{A.10}$$

$$Z_{500} = \frac{R(\overline{T}_a + T_0')}{g}\left[ln\left(1 + \frac{p'_{surface}}{1000}\right) + ln2\right] \tag{A.11}$$

With $\frac{p'_{surface}}{1000} << 1$ it is possible to use the following relationship $ln\left(1+\frac{p'_{surface}}{1000}\right) \approx \frac{p'_{surface}}{1000}$.

$$Z_{500} \approx \frac{R(\overline{T}_a + T'_0)}{g}\left[\frac{p'_{surface}}{1000} + ln2\right] \tag{A.12}$$

Equation A.12 is possible to expand, and the squared perturbation terms could be neglected. This yields

$$Z_{500} \approx \frac{R\overline{T}_a}{g}ln2 + \frac{RT'_0}{g}ln2 + \frac{R\overline{T}_a}{g}\frac{p'_{surface}}{1000} \tag{A.13}$$

As seen in equation A.8, we can expand the pressure term into a mean and pertubed part. This means thet we can expand the 500 hPa pressure surface into $Z_{500} = \overline{Z}_{500} + Z'_{500}$. The mean state is

$$\overline{Z}_{500} = \frac{R\overline{T}_a}{g}ln2 \tag{A.14}$$

By using the equations A.14 and A.13, the following equation is derived

$$Z_{500} \approx \bar{Z}_{500}\left(\frac{T'_0}{T_a} + \frac{1}{ln2}\frac{p'_{surface}}{1000}\right) \tag{A.15}$$

Which equals

$$Z_{500} - \overline{Z}_{500} = Z'_{500} \approx \bar{Z}_{500}\left(\frac{T'_0}{T_a} + \frac{1}{ln2}\frac{p'_{surface}}{1000}\right) \tag{A.16}$$

A.3 Statistical methods

A.3.1 Mean

The mean of an empirical distribution is given by

$$\overline{X} = \frac{1}{n} \sum_{i=1}^{n} x_i \tag{A.17}$$

which is the arithmetic mean of the observations $x_1, x_2, x_3, ..., x_n$ Hogg & Tanis (2010)

A.3.2 Standard deviation

The standard deviation is a measure of the variance in a data set. The relationship between the variance and the standard deviation as given in Hogg & Tanis (2010)

$$VAR(X) = \sigma^2 \Rightarrow \sigma = \sqrt{VAR(X)} \tag{A.18}$$

Where σ^2, also denoted as $VAR(X)$ is the variance, and σ is the standard deviation given by

$$\sigma = \sqrt{\frac{1}{n-1} \sum_{i=1}^{n} (x^i - \overline{x})^2} \tag{A.19}$$

A.4 Supplementary figures

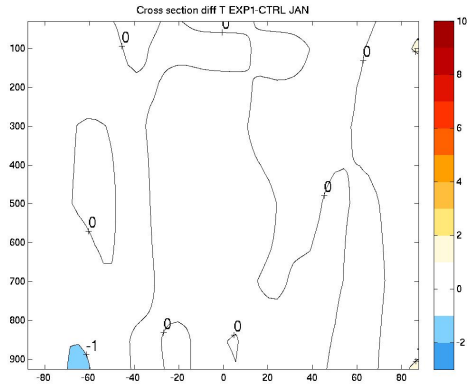

(a) T JAN

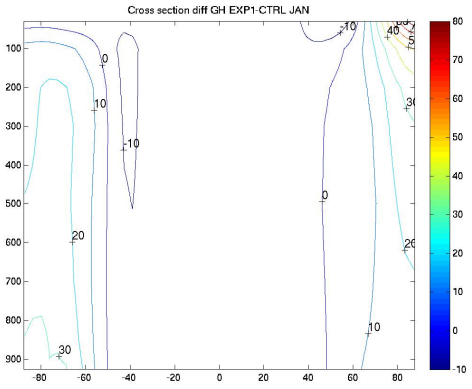

(b) GH JAN

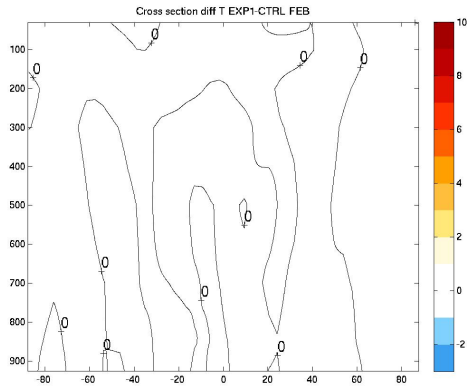

(c) T FEB

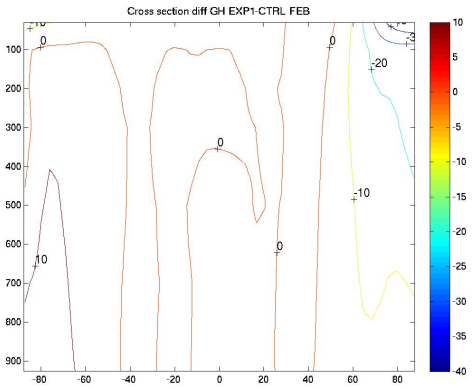

(d) GH FEB

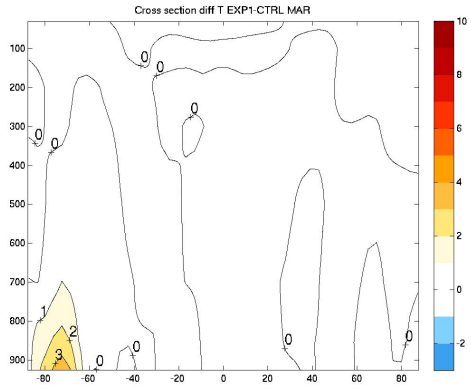

(e) T MAR

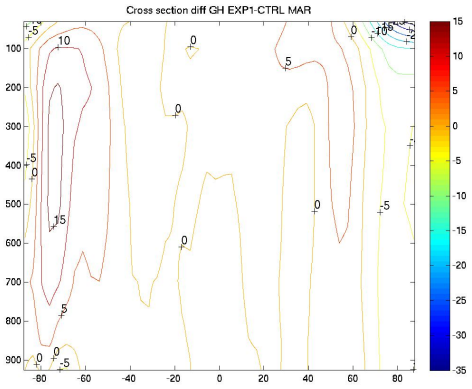

(f) GH MAR

Figure A.1: Latitude (x-axis) - pressure (y-axis) cross section of the monthly mean zonal-mean response in temperature [^{o}C] (left) and geopotential height [m] (right). January to March are shown.

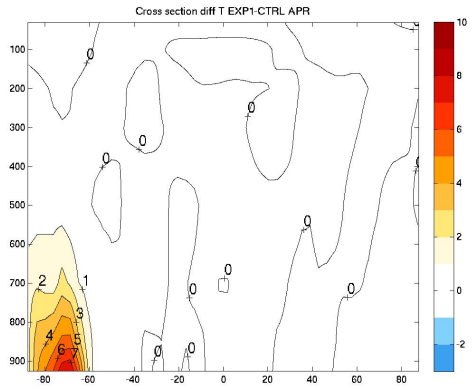

(a) T APR

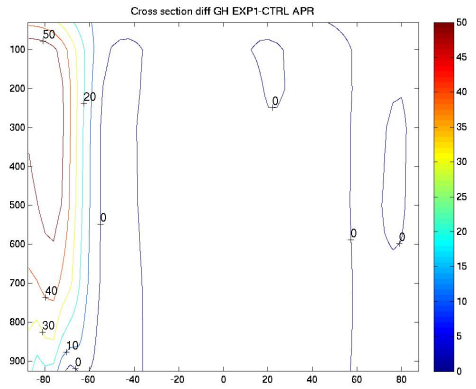

(b) GH APR

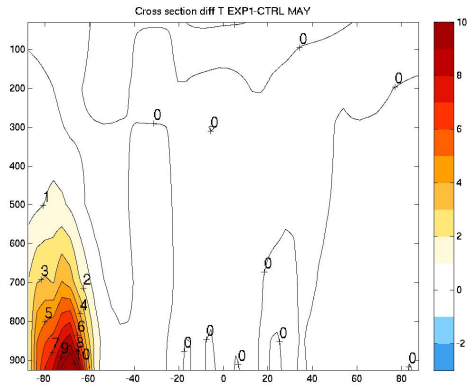

(c) T MAY

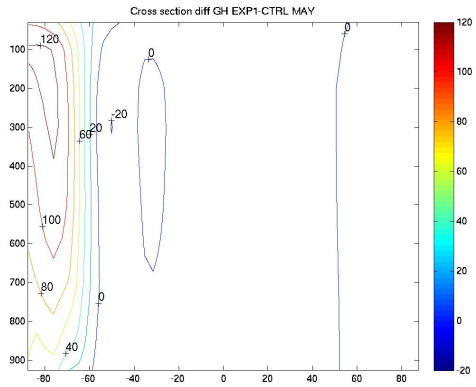

(d) GH MAY

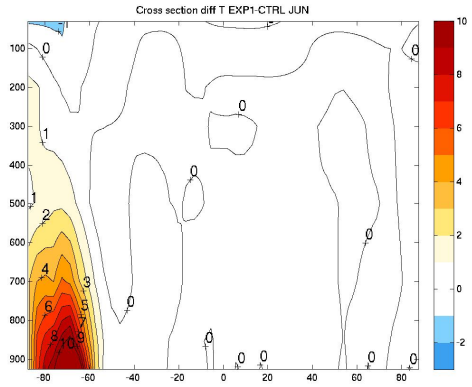

(e) T JUN

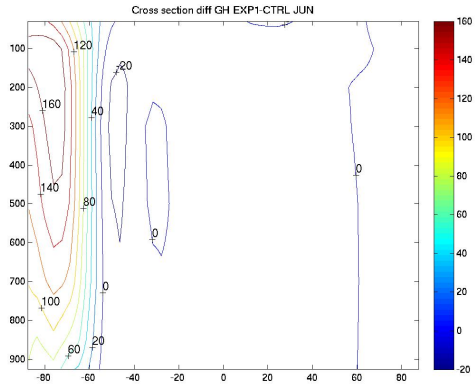

(f) GH JUN

Figure A.2: Same as figure A.1, but for April to June.

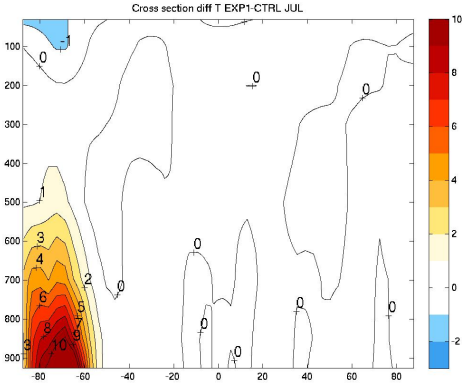

(a) T JUL

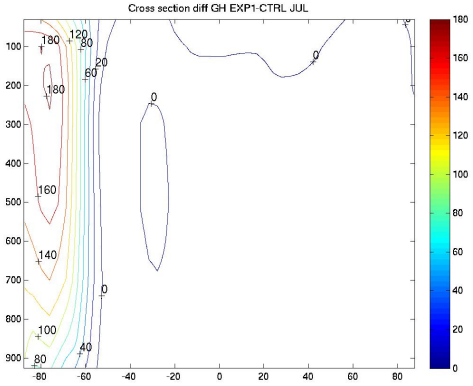

(b) GH JUL

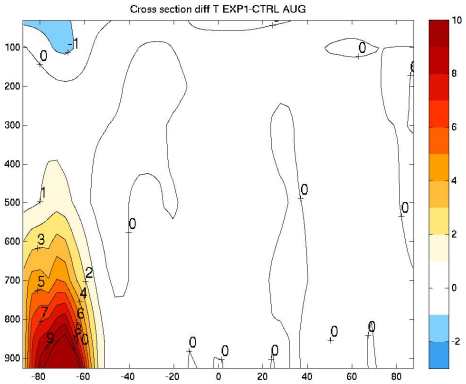

(c) T AUG

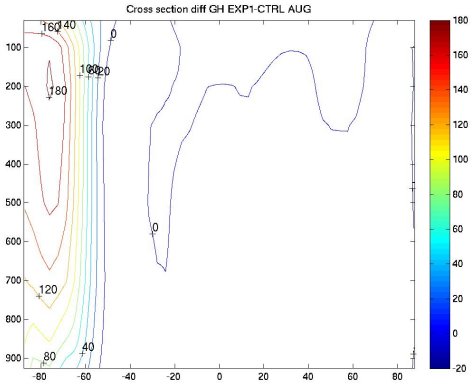

(d) GH AUG

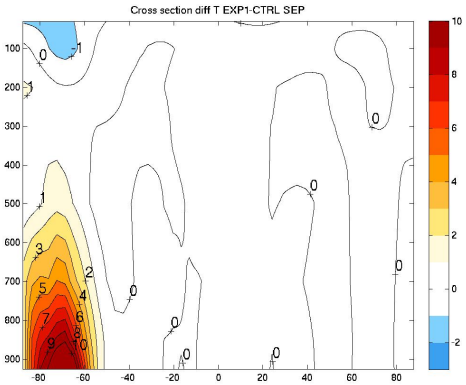

(e) T SEP

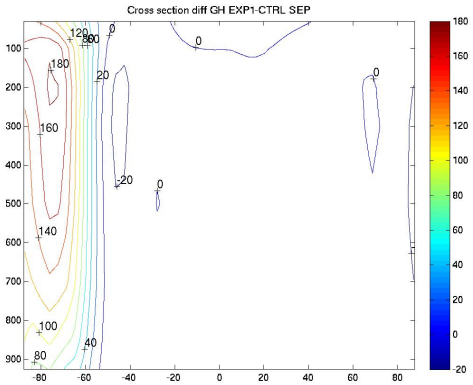

(f) GH SEP

Figure A.3: Same as figure A.1, but for July to September.

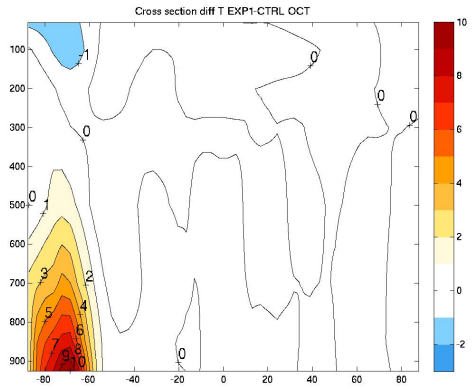

(a) T OCT

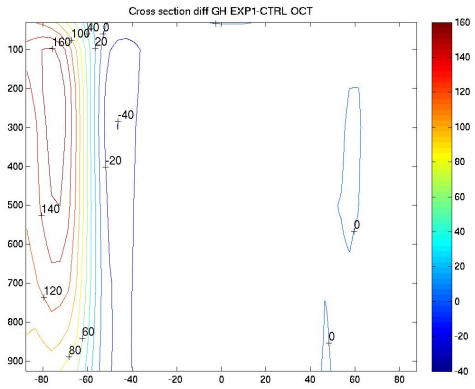

(b) GH OCT

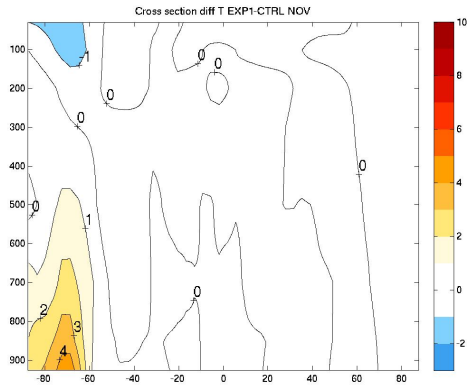

(c) T NOV

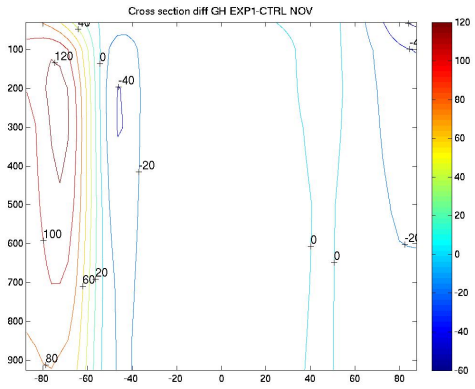

(d) GH NOV

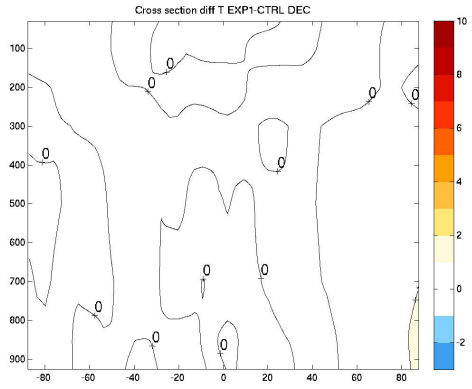

(e) T DEC

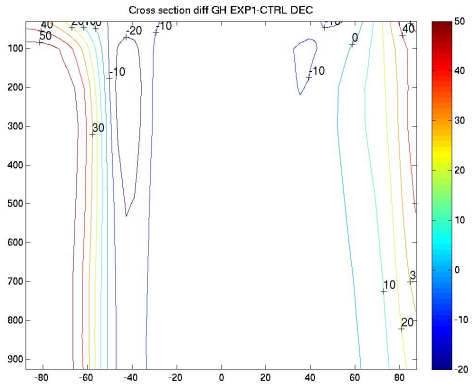

(f) GH DEC

Figure A.4: Same as figure A.1, but for October to December

Bibliography

Arblaster, J. M. 2006. Contributions of external forcings to Southern Annular Mode trends. *Journal of Climate*, **19**(12), 2896.

Bader, J., & Latif, M. 2005. North Atlantic oscillation response to anomalous Indian Ocean SST in a coupled GCM. *Journal of Climate*, 5382–5389.

BCCS. 2010. http://www.bccs.uni.no/units/parallab. *Last visited 25.05.2010*, **2010**.

Bromwich, D. H. 1998. Global atmospheric impacts induced by year-round open water adjacent to Antarctica. *Journal of geophysical research*, **103**(d10), 11173.

Bromwich, D.H., Tzeng, R.Y., & Parish, T. R. 1994. Simulation of the Modern Arctic Climate by the NCAR CCM1. *Journal of Climate*, **7**(7), 1050–1069.

Bromwich, D.H., Chen, B., & Tzeng, R.Y. 1995. Arctic and Antarctic precipitation simulations produced by the NCAR community climate models. *Annals of Glaciology*, **21**, 117–122.

Codron, F. 2007. Relations between Annular Modes and the Mean State: Southern Hemisphere Winter. *Journal of the Atmospheric Sciences*, **64**(9), 3328–3339.

ECMWF. 2009. http://www.ecmwf.int/. *Last visited 25.10.2009*, **2009**.

Fagerli, S.A. 2008. *Atmospheric response to zonally averaged sea surface temperatures in the North Atlantic: a model study*. Ph.D. thesis, UiB.

Flugge, M. 2009. *Simulated atmospheric response to decreased Antarctic sea-ice extent: a model study*. Ph.D. thesis, UiB.

Garreaud, RenÃ©D., & Battisti, David S. 1999. Interannual (ENSO) and Interdecadal (ENSO-like) Variability in the Southern Hemisphere Tropospheric Circulation*. *Journal of Climate*, **12**(7), 2113–2123.

Hartmann, D. L. 1994. *Global Physical Climatology*. Academic Press.

Hogg, Robert V., & Tanis, Elliot A. 2010. *Probability and statistical inference*. Upper Saddle River, N.J.: Pearson/Prentice Hall. 8th ed.

Holton, J. R. 2004. *An Introduction to Dynamic Meteorology*. Elevier.

Hoskins, B. J., & Karoly, D.J. 1981. The steady linear response of a spherical atmosphere to thermal and orographic forcing. *Journal of the Atmospheric Sciences*, **38**(6), 1179.

IPCC. 2007. Climate Change 2007: Synthesis Report - AR4 Synthesis Report. *http://www.ipcc.ch/ Last visited 25.05.2010*.

Kidson, J. W. 1988. Indices of the Southern Hemisphere zonal wind. *Journal of Climate*, **1**(2), 183.

Kucharski, F., & Molteni, F. 2006. Description of the ICT AGCM (SPEEDY) - Version 40. *Speedy documentation*.

Kushnir, Y, Robinson, W. A, Blad, I, Hall, N. M. J, Peng, S, & Sutton, R. 2002. Atmospheric GCM Response to Extratropical SST Anomalies: Synthesis and Evaluation. *Journal of Climate*, **15**(16), 2233–2256.

Limpasuvan, V., & Hartmann, D. L. 1999. Eddies and the annular modes of climate variability. *Geophys. Res. Lett.*, **26**(20), 3133–3136.

Lorenz, E.N. 1956. Empirical orthogonal functions and statistical weather prediction. *Scientific Report 1*.

Molteni, F. 2003. Atmospheric simulations using a GCM with simplified physical parametrizations. I: Model climatology and variability in multi-decadal experiments. *Climate dynamics*, **20**(2), 175.

Nigam, & DeWeaver. 2003. Stationary Waves (Orographic and Thermally forced). *Encyclopedia of Atmospheric Sciences*.

Peters, D., & Waugh, D.W. 2003. Rossby Wave Breaking in the Southern Hemisphere Wintertime Upper Troposphere. *Monthly Weather Review*, **131**(11), 2623–2634.

Rogers, J. C. 1982. Spatial variability of sea level pressure and 500 mb height anomalies over the Southern Hemisphere. *Monthly Weather Review*, **110**(10), 1375.

Seierstad, I. A., & Bader, J. 2009. Impact of a projected future Arctic Sea Ice reduction on extratropical storminess and the NAO. *Climate dynamics*, **33**(7-8), 937.

Smith, S. R., & Stearns, C. R. 1993. Antarctic Pressure and Temperature Anomalies Surrounding the Minimum in the Southern Oscillation Index. *J. Geophys. Res.*, **98**(D7), 13071–13083.

SPEEDY-Net, ICTP Atmospheric General Circulation Model. 2006. http://users.ictp.it/ kucharsk/speedy-net.html. *Last visited 26.05.2010*.

Stull, R. B. 1989. *An introduction to boundary layer meteorology*. Dordrecht: Kluwer Academic Publishers. 2nd reprint.

Tao, X., Walsh, J. E., & Chapman, W. L. 1996. An Assessment of Global Climate Model Simulations of Arctic Air Temperatures. *Journal of Climate*, **9**(5), 1060–1076.

Thompson, D.W.J., & Wallace, J.M. 2000. Annular modes in the extratropical circulation. Part I: Month-to-month variability. *Journal of Climate*, **13**(5), 1000.

Tzeng, R.Y., Bromwich, D.H., Parish, T.R., & Chen, B. 1994. NCAR CCM2 simulation of the modern Antarctic climate. *J. Geophys. Res.*, **99**(D11), 23131–23148.

Tzengo, R.Y., Bromwich, D. H., & Parish, T.R. 1993. Present-Day Antarctic Climatology Of the NCAR Community Climate Model Version 1. *Journal of Climate*, **6**(2), 205–226.

Wallace, J. M. 1977. *Atmospheric science : an introductory survey / John M. Wallace, Peter V. Hobbs*. Elevier.

Washington, W. M., & Parkinson, C.L. 1986. *An introduction to three-dimensional climate modeling / Warren M. Washington, Claire L. Parkinson*. Oxford University Press.

Weller, J. 2010. http://www.lastocean.com/. *Last visited 30.10.2009*, **2009**.

Xu, J.S., von Storch, H., & Loon, H. 1990. The Performance of Four Spectral GCMs in the Southern Hemisphere: The January and July Climatology and the Semiannual Wave. *Journal of Climate*, **3**(1), 53–70.